Materials Characterization 193 (2022) 112293

Contents lists available at ScienceDirect

Materials Characterization

journal homepage: www.elsevier.com/locate/matchar

EBSD analysis of strain distribution and evolution in ferritic-Pearlitic steel under cyclic deformation at intermediate temperature

Shutong Zhang [a], Sebastian Romo [a,b], Rafael A. Giorjao [a], Pablo B.P. Leao [a,c], Antonio J. Ramirez [a,*]

[a] The Ohio State University, Materials Science and Engineering Department, Columbus, OH, USA
[b] Institución Universitaria Pascual Bravo, Facultad de Ingeniería, Medellín, Colombia
[c] Universidade Federal do Ceará, Department of Metallurgical and Materials Engineering, Fortaleza, Brazil

ARTICLE INFO

Keywords:
Low-cycle fatigue
EBSD
Nanoindentation
Strain localization
KAM
GROD

ABSTRACT

Strain accumulation as a result of cyclic loading affects the microstructure and mechanical performance of low-alloy steels under cyclic operation condition. This manuscript presents a comprehensive analysis of a ferritic-pearlitic SA204 Grade C steel under strain-controlled low-cycle fatigue tests to understand the microstructural deformation and strain localization in the ferritic-pearlitic steel. Low-cycle fatigue tests were performed in a Gleeble® thermo-mechanical simulator at 0.008, 0.01, 0.015, and 0.02 strain amplitudes under an isothermal condition at 250 °C. The microstructure evolution during cyclic loading was evaluated using the samples from interrupted 0.01 strain amplitude tests. The LCF analysis shows strain localization at the ferrite-cementite interfaces and ferrite-pearlite interfaces. The characterization results using OM, SEM, EBSD, and nanoindentation analysis reveals the grain misorientation in the ferritic-pearlitic microstructure due to strain accumulation increases with the strain amplitudes and the loading cycles.

1. Introduction

Ferritic-pearlitic steels are used as a structural material for a wide range of applications, such as infrastructure and transportation applications. It possesses a good combination of strength and ductility from the duplex microstructural constituents. The mechanical performance of ferritic-pearlitic steel can be predicted based on a mixture law of ferrite and pearlite microstructures and their volume fractions [1]. Hot-rolled medium carbon steel typically exhibits a pearlite band structure along the rolling direction due to the segregation of Mn and Si [2–6]. The distribution of pearlite in the steel matrix affects the mechanical behavior and crack growth resistance of ferritic-pearlitic steels [6–10]. At the *meso* level, the different micro-mechanical properties of ferrite and pearlite lead to strain partitioning under plastic deformation [11,12]. Plastic strain localization may occur at cementite-ferrite and ferrite-pearlite interfaces [12]. However, the strain localization observed in ferritic-pearlitic steel is considered lower than in ferritic-martensitic and ferritic-bainitic steel because the mechanical properties difference between the soft and the hard microstructural components is lower than the later ones [13]. Strain distribution in lamellar pearlite is affected by the inter-lamellar spacing and the angle between the lamellar cementite orientation and the tensile stress direction [12,14]. Izotov et al. showed that finer pearlite colonies with narrow inter-lamellar distance increase the strain hardening ratio of monotonic loading and avoid crack initiation at the ferrite-lamellar interface [12]. The flow stress and strain hardening in pearlitic steels are related to the mean free path of dislocations on the slip plane in the ferrite phase [15,16]. Cementite interlayers prevent the dislocation motion on the BCC slip plane and lead to an increase in dislocation density [17]. As a result, the dislocation pileup enhances the strain-hardening of pearlite until the shearing of cementite plates.

During cyclic loading, the incompatibility within the duplex microstructures enhance the plastic strain within the softer microstructural constituent. The significant incompatibility in ferrite-martensite microstructure compromises fatigue crack resistance [18]. A crystal plasticity model developed by Zecevic et al. showed that geometrical necessary dislocations (GNDs) accumulate at the ferrite-martensite interface during cyclic deformation, leading to the localized hardening in the ferrite grains [19]. Strain localization at the interface between the hard and soft microstructural constituents also promotes crack

* Corresponding author.
E-mail address: ramirez.49@osu.edu (A.J. Ramirez).

https://doi.org/10.1016/j.matchar.2022.112293
Received 18 June 2022; Received in revised form 17 August 2022; Accepted 6 September 2022
Available online 11 September 2022

formation. Narasiah and Ray pointed out that ferritic-pearlitic interfaces are a preferential spot for short crack nucleation under cyclic loading [20]. In addition, the increasing GNDs at both ferrite and pearlite contribute to the hardening instead of just the soft ferrite grain in a ferrite-martensite steel. Liu et al. revealed that misorientation increases in the proeutectoid ferrite and the ferrite phase in pearlite during the rolling contact fatigue [21]. Strain amplitude could influence the cyclic response of ferritic-pearlitic steels by increasing the plastic deformation in each cycle [22,23]. Sankaran et al. showed that ferritic-pearlitic steel exhibits cyclic hardening at higher total strain amplitudes ($\geq$ 0.7%) and cyclic softening at lower strain amplitudes ($<$ 0.7%) [24]. In addition, the impact of dual-microstructure upon retarding fatigue crack propagation has been reported in ferrite-martensite steels [25]. Fatigue crack growth is less retarded in the ferritic-pearlitic steel than ferritic-bainitic steel. However, the ferritic-pearlitic microstructure could still effectively increase the tortuosity of the crack path [17,26]. Small and densely distributed pearlites are more favorable to increasing crack tortuosity than large-size pearlites [27]. Uniformly distributed pearlite structure possesses higher fatigue crack growth resistance than banded pearlite structure by reducing the plastic zone of crack tips and increasing the crack path tortuosity [28–30].

Electron backscattering diffraction (EBSD) has been widely used to reveal microstructural deformation [31–36]. The Kernel Average Misorientation (KAM) and the Grain Reference Orientation Deviation (GROD) maps from Rui et al. show the impact of stress ratio and stress intensity factor on the final misorientation along the crack tip under cyclic loading [37]. Rae et al. demonstrated that the misorientation angle of 12% Cr martensitic steel reduces during the cyclic softening of fatigue [38]. In addition, EBSD analysis of deformation could be performed in combination with nanoindentation measurements to reveal the local hardening caused by strain localization [34,35,39]. Githinji et al. showed that the EBSD analysis exhibits good agreement with nanoindentation in evaluating the service-aged 316 austenitic steel deformation [34]. High throughput nanoindentation measurements performed by Chang et al. demonstrated the effective correlations between EBSD analysis and nanoindentation measurements in the complex-phase steel [40].

Although the dual-constituent steel microstructure exhibits a similar strain hardening mechanism under monotonic and cyclic tension-compression loadings, different dislocation motions due to the loading condition result in a change of damage accumulation within the microstructure. The consistent tensile direction under monotonic loading leads to continuous and directional dislocation motion along the activated slip planes. In contrast, the dislocation motion occurs reversibly under cyclic tension-compression. Steels under monotonic loading exhibit a more pronounced strain hardening effect than under cyclic loading. However, the accumulation of dislocation density is much larger in a cyclically-deformed microstructure [41]. During the saturated cycles, stable dislocation cells form within the microstructure, and the cyclic stress becomes stabilized, irrelevant to the plastic strain. Many studies have been published to characterize the monotonic deformation of dual-constituent steel microstructure using EBSD analysis [31,39,42]. However, few address the impact of fatigue strain amplitudes and microstructural evolution under cyclic loading conditions. This study will provide a comprehensive characterization of the micro-scale deformation in ferritic-pearlitic low-alloy steel under low-cycle fatigue. The studied material is C-0.5Mo steel, which belongs to SA 204 Grade C according to the ASME Boiler and Pressure Vessel Code Section II Part A [43]. Mo content was added to the low-alloy steel to improve the creep resistance at elevated temperatures. The material has been widely adopted as the base material for coke drums, which are large pressure vessels that render the thermal cracking of heavy oil molecules into lightweight products. During each operation cycle, heating and quenching of coke drums occur within a temperature range from 100 °C to 480 °C, which generates internal stresses and leads to severe plastic deformation [44–46]. The study aims at elucidating the performance and microstructural deformation of the C-0.5Mo steel base metal with ferritic-pearlitic microstructure under cyclic deformation. An isothermal condition was selected at 250 °C to represent the intermediate temperature at which the largest plastic deformation occurs in coke drums. Stress induced by mechanical loading was used to mimic the thermal stress that occurs in coke drums. Hence, low-cycle fatigue tests at high strain amplitudes, including 0.008, 0.01, 0.015, and 0.02, were implemented to induce cyclic deformation within the duplex microstructure constituents. However, the experiment goal was not to fully replicate the coke drum operation condition but to create a reliable approach to evaluate materials performance and microstructural changes for coke drum and similar applications. In addition, the microstructure evolution was investigated in the samples from interrupted fatigue tests at 0.01 strain amplitude. EBSD and nanoindentation measurements of the fatigue samples and the interrupted samples were performed to elucidate the microstructure effect upon the strain localization within the ferritic-pearlitic microstructure and the connection between the microstructure evolution and the mechanical performance of the ferritic-pearlitic steel.

2. Method and approach

2.1. Microstructure characterization

The evaluated C-0.5Mo steel was procured as steel plates in a normalized condition. The dimension of the steel plates was 305 mm × 305 mm × 38 mm. The bulk chemical composition of the As-Received material was measured using optical spectrometry, as shown in Table 1.

Metallography samples were sectioned from the As-Received material and the gauge sections of fatigue samples and then mounted in conductive bakelite. The surface of each sample was ground using 240, 400, 600, 800, and 1200 grit SiC paper and polished using diamond paste (6 μm and 1 μm) and colloidal silica (0.02 μm). The steel microstructure was etched with 2.0% Nital etchant (2.0% Nitric acid and 98% ethanol) and characterized using optical microscopy (OM) and Apreo Scanning electron microscope (SEM). The secondary SEM images used 10 kV accelerating voltage and 3.2 nA beam current. The grain size, including ferrite and pearlite, was measured quantitatively using electron backscatter diffraction (EBSD) analysis. The grain size distributions were measured in two different regions of a fatigue sample using the OIM analysis software. Grain distributions from two measurements were combined to calculate the average grain size and standard deviation based on the mixture of normal distributions. In addition, the average ferrite-pearlite fraction was measured using OM at 200× magnification in 10 different fields. The images were processed to a binary format to differentiate the ferrite and pearlite colonies and measured by pixels using the Image J software [47].

2.2. Isothermal low-cycle fatigue test

Isothermal low-cycle fatigue (ILCF) tests were performed in the Gleeble thermo-mechanical simulator. The ILCF tests were strain-controlled fully-reversed tests at 0.008, 0.01, 0.015, and 0.02 strain amplitudes ($\Delta\varepsilon_{tot}/2$). The test temperature was maintained at 250 °C through resistance heating of the sample gauge section. The strain rate is controlled at 0.002/s, and the signal sampling rate is 10 Hz. Dog-bone-shaped samples were machined parallel to the rolling direction within the 13 mm thickness (1/3 plate thickness) from the top surface of steel plates. This was designed to avoid the change of mechanical properties caused by banded structures that form in the middle of the plate due to Mn and Si segregations [48–50]. Cyclic responses of half stress range ($\Delta\sigma/2$) and inelastic energy density (ΔW) were evaluated at the different strain amplitudes. The plastic strain amplitude ($\Delta\varepsilon_p/2$) and inelastic energy density (ΔW) can be calculated based on the cyclic stress-strain loop shown in Fig. 1 to represent the plastic deformation per cycle. Experimental data of plastic strain and inelastic energy density versus fatigue reversals ($2N_f$) were plotted with the Coffin-Manson Equation

Table 1
Chemical composition in wt% of C-0.5Mo steel measured by optical spectrometer.

#	C	Mn	P	S	Si	Fe	Mo	Cr	Ni	Cu
C-0.5Mo steel	0.2	0.7	0.01	0.01	0.21	Bal.	0.48	0.09	0.11	0.16

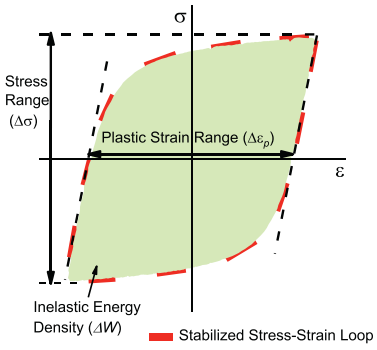

Fig. 1. Schematic of stabilized stress-strain loop. Inelatic energy density (ΔW) is defined as the internal area of a cyclic stress-strain loop.

and the energy-based model [51–53].

2.3. EBSD analysis of fatigue samples and interrupted test samples

EBSD analysis was performed to characterize the microstructure of As-Received and fatigue samples tested at 0.008, 0.01, 0.015, and 0.02 strain amplitudes. The microstructural evolution of the ferritic-pearlitic microstructure was investigated using the interrupted test samples of the 5th cycle, 30th cycle, and 300th cycle during cyclic tests at 0.01 strain amplitude. The accelerating voltage and beam current used for EBSD analysis were 20 kV and 6.4 nA. The EBSD scanning step size was 0.2 μm, and the scanning area was 150 μm × 120 μm. The pre-selected scanning regions were surrounded by micro-hardness indentations. Inverse pole figure (IPF), kernel average misorientation (KAM), and grain reference orientation deviation (GROD) of analyzed regions were obtained using the OIM software. All the IPF maps were plotted in the normal direction (ND), and the rolling direction is (RD) parallel to the loading dirction. KAM is a kernel-based approach to revealing the local misorientation within the microstructure. The KAM values within the grains were calculated based on the average misorientation of one point and its first nearest neighbors, which have a misorientation of $<5°$. The KAM is shown to be directly related to the GNDs that form to accommodate the accumulation of plastic strain [36]. On the other hand, GROD calculates misorientation using a reference of the average misorientation value within a grain. The GROD value reflects the orientation deviation within grains caused by the strain localization. The EBSD results from different conditions were summarized in graph tables to reveal the impact of strain amplitude and loading cycles on microstructural deformation. In addition, the fatigue cracks close to 0.01 strain sample surface were analyzed to reveal the microstructural impact upon crack initiation and propagation.

Grain-based KAM and GROD analyses were performed to quantitatively evaluate the microstructural deformation within the ferrite-pearlite microstructure under different conditions. The grain IDs within the analyzed microstructure region were labelled using the OIM software, and the average KAM and GROD values were calculated to gain a statistical analysis of the grain-based misorientation. Tolerance angle and minimum grain size were used as partition parameters to optimize grain identification. The tolerance angle was used to define the grouping of pixels as grains. As is shown in Fig. 2 (a), the average grain size increases with the tolerance angle. A small tolerance angle setting induces the misindexing of pearlitic ferrite and dislocation cells as grains and confuses the grain-based misorientation values. On the other hand, a large tolerance angle setting merges some of the pearlite colonies with the neighboring ferrite grains bounded by low-angle GBs. Therefore, the optimization strategy was selecting an appropriate tolerance angle that correctly separates the major ferrite-pearlite grains and then using a universal grain size threshold at 1.5 μm to eliminate the misindexed fine grains, as is shown in Fig. 2 (b). The tolerance angle and minimum grain size adopted for each sample were summarized in Table 2.

2.4. Nanoindentation measurements

Nanoindentation measurements of As-Received and deformed microstructure were performed using an XP-Nano instrumented indentation system. A Berkovich diamond indenter was used to measure the hardness of the microstructure. A load-control mode was used with 20 mN maximum load and 5 s holding time. An indent grid of 15 × 10 (150 indentations) was adopted with a 20 μm spacing in both x and y directions. The indented samples were etched with 2.0% Nital etchant, and each indent was labelled with microstructure constituents based on

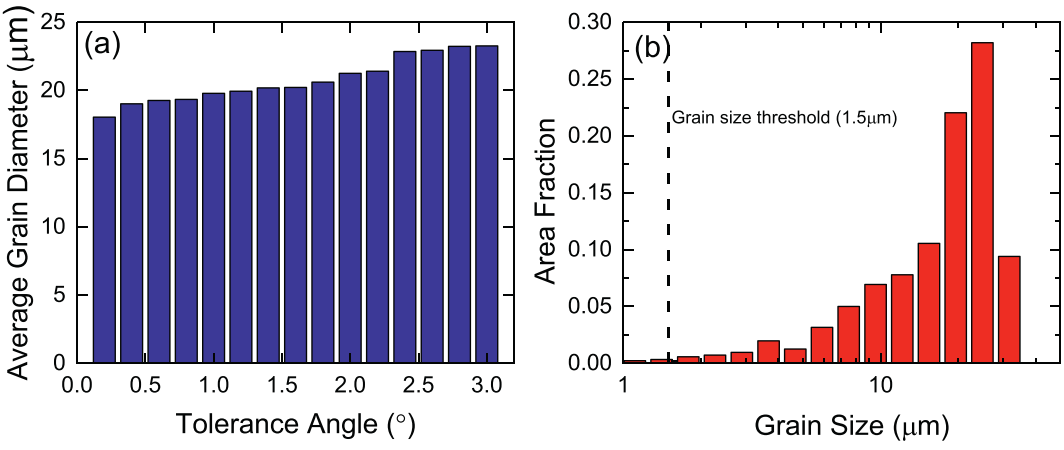

Fig. 2. Partition parameters optimization for grain-based analysis of fatigue sample at 0.01 strain. (a) Tolerance angle and average grain diameter. (b) Area fraction distribution of grain size at 1° tolerance angle.

Table 2
Summary of partition parameters for grain-based analysis.

Parameters	As-received	Fatigue samples				Interrupted test samples ($\Delta\varepsilon/2 = \pm 0.01$)		
		0.008	0.01	0.015	0.02	5 cycle	30 cycle	300 cycle
Tolerance angle (°)	0.6	0.6	0.8	1	2	0.7	0.65	0.8
Minimum grain size (μm)	1.5	1.5	1.5	1.5	1.5	1.5	1.5	1.5

the visual check with OM. Due to the spatial resolution of the nanoindentation, the indents located at the ferrite-pearlite interface exhibited a significant hardness variation, thus they were not considered in the analysis. Fig. 3 shows the load-displacement curves of two nanoindentation measurements among the indentation array of the As-Received sample. The indented microstructure hardness values were calculated based on the measured load-displacement curves.

3. Results

3.1. Microstructure characterization

Fig. 4 shows the SEM secondary electron (SE) images of ferritic-pearlitic microstructure in the C-0.5Mo low-alloy steel. Evenly distributed pearlite structure is observed in the steel matrix of fatigue samples without significant segregation bands forming. Fig. 5 (a) shows the inverse pole figures of one of the two analyzed regions, which were randomly selected within the as-received microstructure close to the region in Fig. 4 (a). Fig. 5 (b) shows the distribution of grain size based on area fractions. The calculated average grain size based on area fraction is 22.23 ± 6.48 μm. In addition, the measured area fractions of ferrite and pearlite were calculated to be 63.4% and 36.6%, respectively, based on the pixel counting of the binary microstructure images.

3.2. Isothermal low-cycle fatigue test

Fig. 6 (a) and (b) show the cyclic responses of half stress range ($\Delta\sigma/2$) and inelastic strain energy density at 0.08, 0.01, 0.015 and 0.02 strain amplitudes. The cyclic stress response of the C-0.5Mo steel samples exhibited hardening within the first ten cycles and then softening to the stabilized condition. Fig. 6 (a) reveals the cyclic stress range response over the loading cycles. The inelastic energy density is more more stable as is shown in Fig. 6(b). Fig. 6(c) shows consistent expansion of the stabilized stress-strain curves, and Fig. 6(d) shows the hardening evolution of the stress-strain curves in the first 3 cycles at 0.02 strain amplitude.

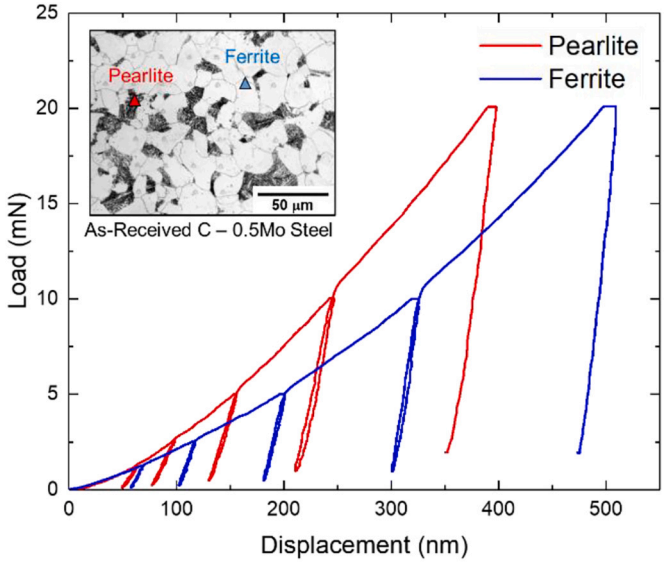

Fig. 3. Load-displacement curves of load-control nanoindentation measurement in ferrite grains and pearlite colonies.

The cyclic hardening ratio, which is defined by the ratio of the maximum stress range and the initial stress range, decreases with increasing strain amplitudes. Plastic deformation per cycle could be represented by the plastic strain amplitude ($\Delta\varepsilon_p/2$) and inelastic energy density (ΔW). Their relationships with fatigue life reversals could be fitted with the Coffin-Manson Equation and the inelastic energy density model, as is shown in Fig. 7(a) and (b) [18]. Both models are in a power-law form, and are able to provide an accurate fitting of the experimental data. Table 3 shows a summary of the parameters extracted from the fatigue tests to obtain Fig. 7. The decreasing cyclic hardening ratio ($\Delta\sigma_{max}/\Delta\sigma_0$) with strain amplitudes indicates that cyclic hardening becomes less prominent under large plastic deformation.

3.3. Nanoindentation measurement of ferritic-pearlitic microstructure

The hardness of ferrite grains and pearlite colonies measured by nanoindentation are shown in Fig. 8. The hardness of pearlite is 80% higher than ferrite in As-Received samples and 40% to 50% higher in fatigue samples. Both ferrite and pearlite in fatigue samples show a hardness increase compared to As-Received samples, but no significant variation was observed among the different strain amplitudes.

Fig. 9 (a) shows the cyclic stress responses of interrupted fatigue tests at 0.01 strain amplitude. Interrupted test samples were obtained at the 5th, 30th, and 300th cycle and the As-Received sample and the failure sample (667th cycle). Nanoindentation measurements were performed to evaluate the microstructure hardness change during the low-cycle fatigue test. As is shown in Fig. 9 (b), the average hardness increases with the cycle number from As-Received to the 300th cycle and decreases at failure. The hardness measurements successfully reveal the cyclic hardening and stabilization of microstructure due to damage accumulation, but the results do not reveal the subtle softening from the 5th to the 30th cycle.

3.4. EBSD analysis of microstructural deformation

3.4.1. Fatigue sample analysis at different strain amplitudes

The EBSD analysis results in Fig. 10 reveal the microstructural deformation in the fatigue samples tested at different strain amplitudes compared to the As-Received sample. The over-imposed grayscale IQ map with the IPF shows the distribution of ferrite grains and pearlite colonies. The KAM images show that the number of ferrite grains with higher misorientation increases with strain amplitudes. At 0.008 and 0.01strain amplitudes, the misorientation is mainly observed in the pearlite colonies and some of the neighboring ferrite grains. Due to heavy cyclic deformation, a significant increase of misorientation in the ferrite grains is observed at 0.015 and 0.02 strain amplitudes. The evaluation of ferrite misorientation in the pearlite colonies using KAM is difficult due to the preexisting misorientation at the ferrite-cementite interfaces. The GROD images show that heterogeneity of crystal orientation within grains increases with strain amplitudes. Gradients of orientation are primarily observed in the vicinity of the ferrite grain boundaries next to the pearlite colonies or grain boundary triple points. At 0.015 and 0.02 strain amplitudes, the crystal orientation deviations in the vicinity of ferrite grain boundaries become significant, indicating a

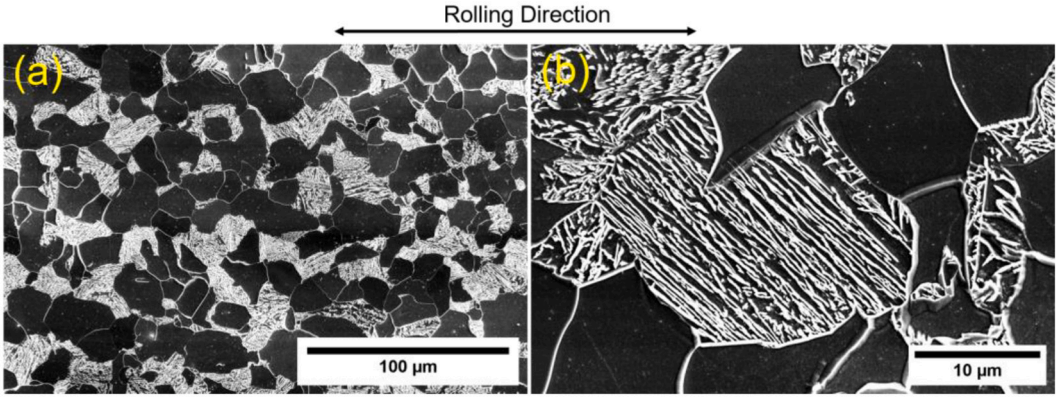

Fig. 4. SEM SE images of ferritic-pearlitic microstructure. (a) Evenly distributed pearlite colonies in the steel matrix. (b) Pearlite colonies structure in detail.

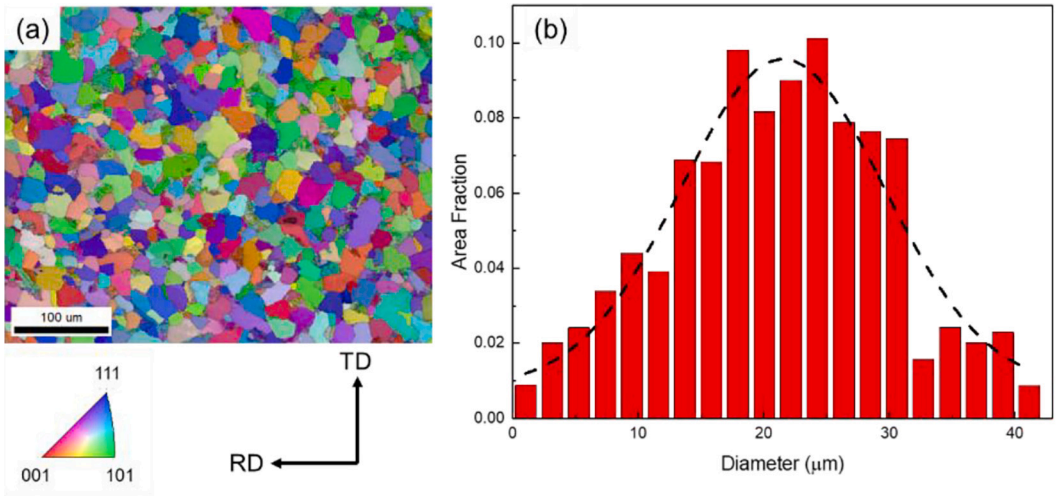

Fig. 5. Ferrite-perlite grain size analysis using EBSD. (a) Inverse pole figure of the scanning region. (b) Histograms of grain size distribution. The IPF map was plotted in the ND direction.

plastic deformation localization due to strain partitioning between the ferrite and pearlite colonies.

Fig. 11 (a)-(d) show the strain localization on a ferrite grain from a sample tested at 0.02 strain amplitude. As shown in Fig. 11 (a) and (b), the ferrite grain is surrounded by neighboring pearlite colonies. Plastic deformation, indicated by low angle grain boundaries, is primarily localized in the regions close to the ferrite grain boundaries. One of the pearlite colonies (indicated by the red arrow in Fig. 11 (a)) with finer inter-lamellar spacing possesses a significant amount of plastic strain, enhancing the strength of pearlite and increasing ferrite-pearlite incompatibility. As a result, strain localization close to the ferrite-pearlite interface is observed in the GROD image, as shown in Fig. 11 (c). An analysis line is drawn from point x to y, and the misorientation result is shown in Fig. 11 (d). The point-to-point misorientation shows the misorienation flunctuations occur within 5 μm distance from the GBs, indicating the strain localization in the vicinity of ferrite-pearlite interface. The point-to-origin misorientation indicates a large variety of crystal orientations between the center region of the ferrite grain and the regions close to the grain boundaries.

3.4.2. *Strain distribution in ferritic-Pearlitic microstructure during fatigue test*

Strain distributions in the ferritic-pearlitic microstructure were evaluated using the interrupted test samples at 0.01 strain amplitude. Fig. 12 shows the IPF, KAM, and GROD mappings of interrupted test samples at the 0th (As-Received), 5th, 30th, 300th, and 667th cycle (failure). The KAM mappings of the as-received, 5th, and 30th cycle samples show that local misorientation is mainly observed in the pearlite colonies. No ferrite grain misorientation is observed in the GROD mappings of the as-received, 5th, and 30th cycle samples. In the 300th and 667th cycle samples, local misorientation is observed in the pearlite colonies and the vicinity of ferrite grain boundaries. The increase of GROD in the vicinity of the ferrite-pearlite grain boundaries indicates the strain localization due to the microstructural incompatibility.

3.4.3. *Strain distribution along crack propagation*

Fig. 13 (a) shows that parallel cracks labelled as C1, C2, and C3 initiated at the ferrite grains on the sample surface. All cracks grew parallel at a 60° angle to the loading direction due to the similar ferrite grain orientation of the initiation grains. These cracks are short cracks confined within a few grains and grow on the primary slip planes of BCC ferrite, which belongs to the stage I fatigue crack growth [25]. C1 and C2 were less deflected during transgranular growth and yielded a kinked shape at grain boundaries. The deflection of C3 crack growth occurred at the grain boundary and diverged to become a forked shape. One of the deflected cracks grew along the direction of the deflecting grain boundary, and the other crack grew into the pearlite colony. Fig. 13 (c) shows a high density of LAGBs accumulates along the crack path into the pearlite colony compared to the low GB density of other cracks in ferrite grains. The KAM image and grain boundary distribution in Fig. 13 (b) and (c) reveal the misorientation along with the crack paths increases along with crack length due to the increasing stress intensity factor [37].

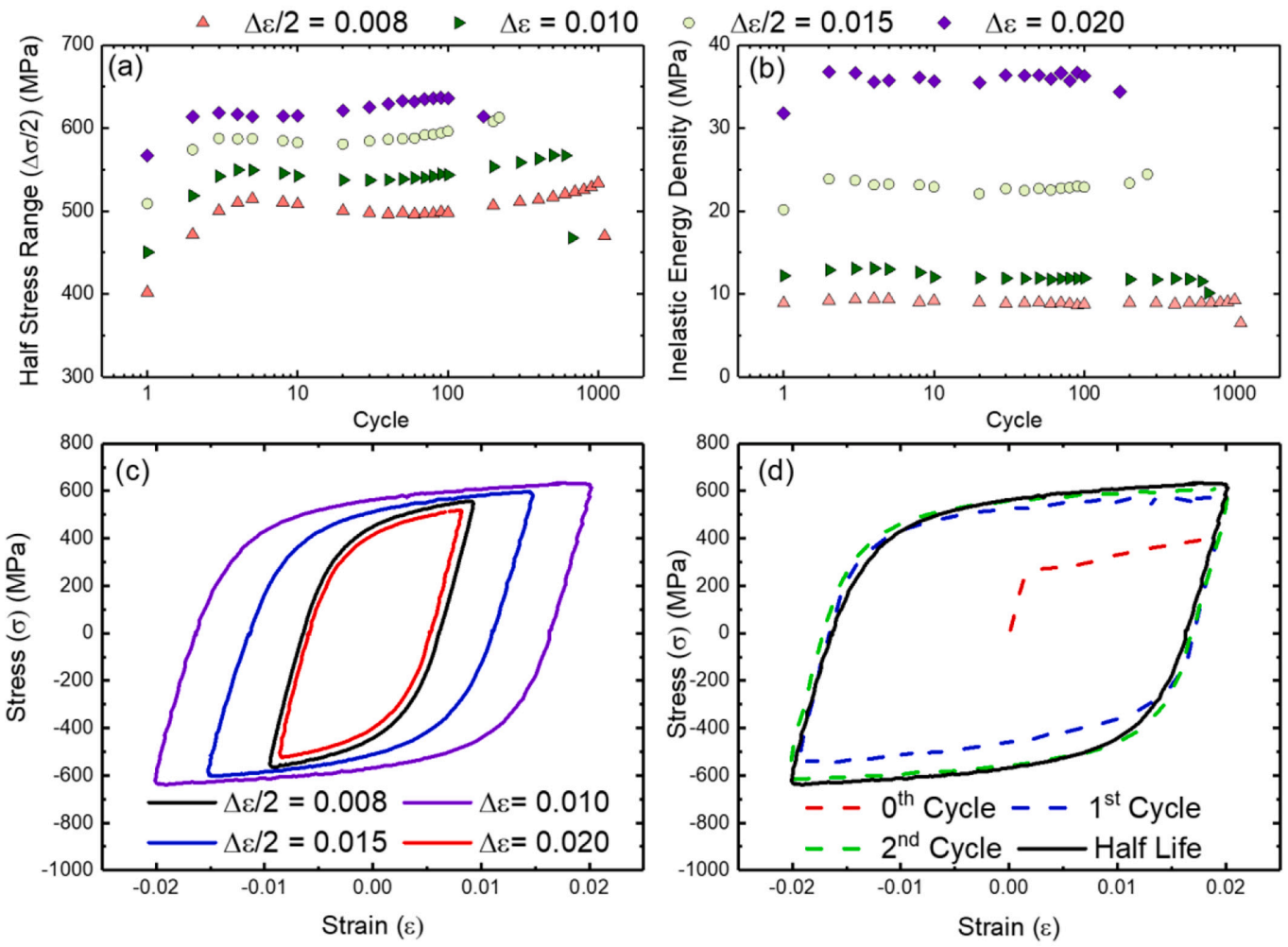

Fig. 6. Summary of low-cycle fatigue results at 0.008, 0.010, 0.015, and 0.020 strain amplitudes. (a) Cyclic response of half stress range (Δσ/2) (b) Cyclic response of inelastic energy density (c) Comparison of stabilized stress-strain curves (d) Evolution of stress-strain curves during cyclic hardening at 0.020 strain amplitude.

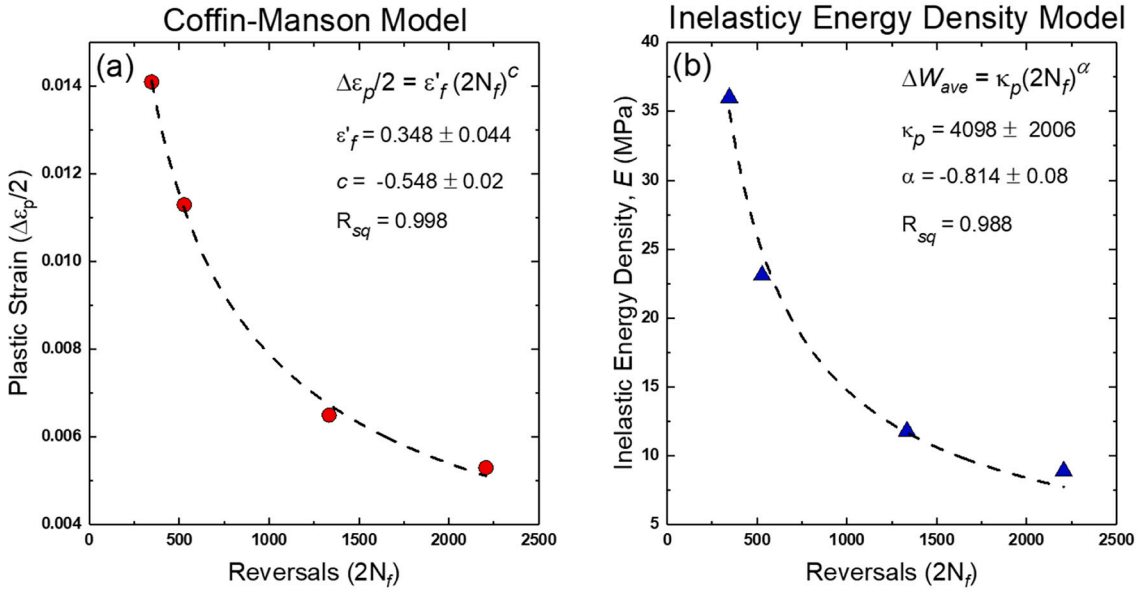

Fig. 7. Relationship between fatigue life and plastic deformation of LCF samples tested at 0.008, 0.01, 0.015, and 0.02 strain amplitudes. (a) Coffin-Manson equation fitting (b) Inelastic energy density model fitting.

Table 3
Summary of ILCF test results.

Strain amplitude ($\Delta\varepsilon/2$)	Stabilized plastic strain amplitude ($\Delta\varepsilon_p/2$)	Average half stress range ($\Delta\sigma/2$) (MPa)	Average inelastic energy density (MPa)	Fatigue life (N_f)	Cyclic hardening ratio ($\Delta\sigma_{max}/\Delta\sigma_0$)	Total accumulative plastic strain
0.008	0.0053	517	8.9	1103	1.57	23.4
0.010	0.0065	558	11.8	667	1.51	17.3
0.015	0.0113	599	23.1	264	1.43	11.9
0.020	0.0141	635	36.0	173	1.25	9.8

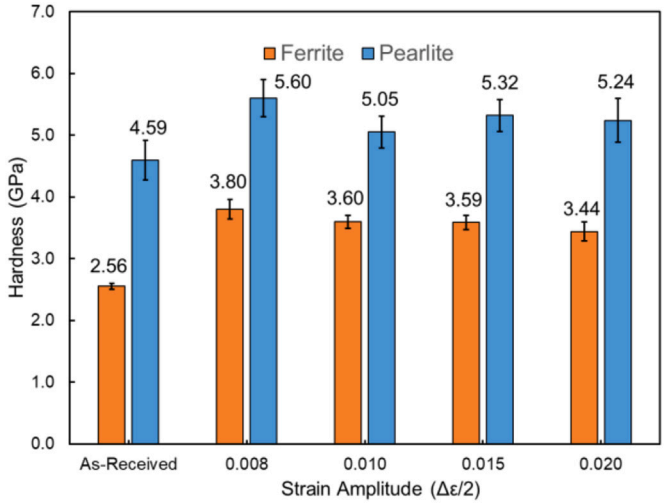

Fig. 8. Nanoindentation measurement of As-Received and fatigue samples tested at 0.008, 0.01, 0.015, 0.02 strain amplitudes. Hardness bar graph of ferrite grains and pearlite colonies. The error bars indicate a 95% confidence interval of the hardness measurements.

The GROD image shows that grain misorientation is distributed along the crack path and close to the grain boundaries.

Fig. 14 (a) shows the IPF figure of a crack propagating in the ferrite grain and deflected at the grain boundary. Sub-grain structure formation is observed along the crack path. The KAM image in Fig. 14 (b) reveals a large amount of misorientation between the crack path and a pearlite colony. Both kernel misorientation and LAGBs distribution indicate plastic strain localization at the ferrite-pearlite interface, where the strength incompatibility is enhanced by the crack plastic zone. The GROD in Fig. 14 (d) reveals that the highest grain misorientation is localized along a deflected crack path close to a pearlite colony.

4. Discussion

4.1. Grain-based analysis of microstructural deformation

According to the EBSD analysis of the ferritic-pearlitic steel, the extent of microstructural deformation increases with the plastic strain amplitudes of LCF tests. The increasing LAGBs in Fig. 15 (a) indicate the increasing strain amplitudes promote the formation of sub-grain walls by GNDs arrangement [54]. The KAM distribution in Fig. 10 shows that the misorientation is mainly distributed in the pearlite colonies of the as-received and the 0.008 strain fatigue sample. However, the strain distribution becomes homogenized at 0.02 strain amplitude regardless of microstructure constituents. This observation in the KAM mapping is consistent with the grain-based analysis in Fig. 15 (b). The KAM distribution of the as-received microstructure exhibits a bimodal distribution, in which the peaks represent the duplex microstructure constituents. However, the KAM distribution becomes unimodal at 0.02 strain amplitude. The significant increase of KAM at 0.02 strain amplitude and strain homogenization in the ferrite grains reveals that multiple slip planes were activated, and dislocation multiplication and interaction occurred to accommodate the heavy plastic deformation. Fig. 15 (c) and (d) show the variation of GB and KAM at the 5th, 30th, 300th, and 667th cycles. The relative frequency of LAGB ($1^\circ \sim 5^\circ$) experiences a subtle decrease from the 5th to the 30th cycle, increases to the 300th cycle, and stays consistent until failure. The variations of LAGB with cycles show good agreement with the change of cyclic stress response in Fig. 9 (a), especially the temporary softening from the 5th to the 30th cycle. The decrease of LAGBs suggests a reduction of dislocation density. Since misorientation is predominantly observed in the pearlite colonies of the interrupted fatigue samples at the 5th and 30th cycles, the change of cyclic stress could be attributed to the softening of pearlite colonies. Paul et al. [55] showed a similar softening effect in dual-phase steels with

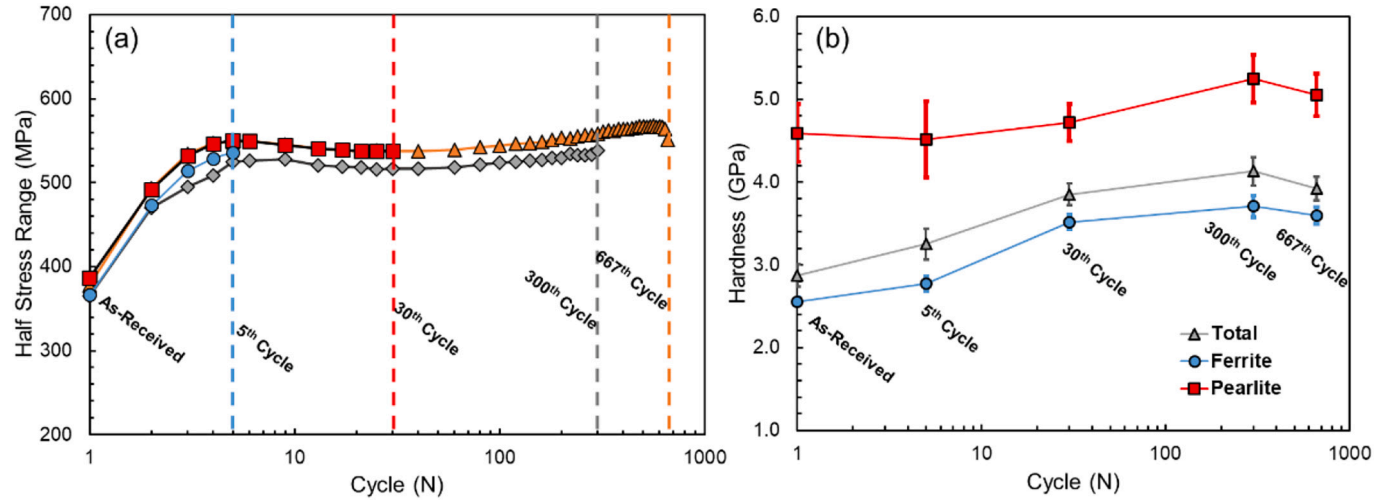

Fig. 9. Cyclic stress range responses of interrupted samples and corresponding hardness evolution. (a) Cyclic response of half stress range during interrupted tests and (b) Microstructure hardness evolution during low-cycle fatigue tests. The error bars indicate a 95% confidence interval of the hardness measurements.

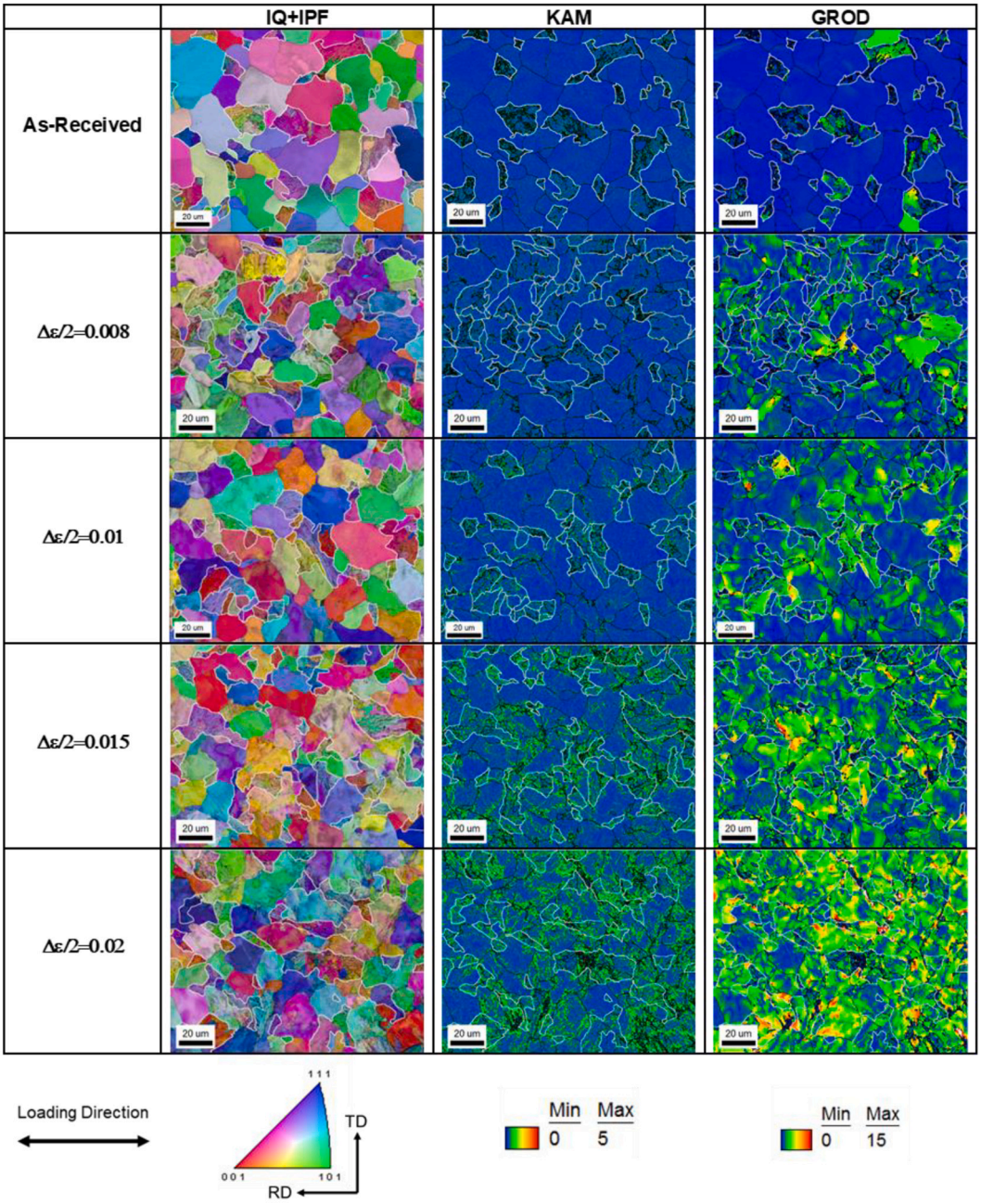

Fig. 10. EBSD analysis of As-Received and fatigue microstructure at different strain amplitudes ($\Delta\varepsilon/2 = 0.008$, 0.01, 0.015 and 0.02). The size of the scanning regions is 150 μm × 120 μm with 0.2 μm step size. The IPF, KAM, and GROD figures show that the accumulation of plastic strain within the ferritic-pearlitic microstructure increases with ILCF strain amplitudes. Pearlite colonies were outlined with white contour. IPF maps were plotted in the ND direction.

20% and 49% martensite content under low-cycle fatigue. According to their study, the cyclic response of the dual-phase steels reveals the competition between ferrite hardening and martensite softening. Nevertheless, considering the subtle LAGB decrease and the small scanning region, temporary softening due to the pearlite softening needs to be further validated with sufficient large areas. In addition, the similar LAGB frequencies at the 300th cycle and the 667th cycle indicate the saturation of dislocations after the cyclic stress stabilized. The KAM increase with cycles is observed in both ferrite grains and pearlite colonies, as indicated by the shift of bimodal peaks from the 5th cycle to the 667th cycle in Fig. 15 (d). However, the reduced spacing of ferrite and pearlite KAM peaks at the 667th cycle indicates an increase of plastic deformation in the ferrite grains over loading cycles. Noh et al. [18] investigated the microstructure evolution of ferritic-pearlitic low-carbon steels during low-cycle fatigue tests using TEM analysis. They showed that the dislocation entanglements were observed in the ferrite grains in the 1st and 3rd cycle, and dislocation cells were observed in the 50th cycle when the strain amplitude was 0.02. Therefore, the KAM mapping does not reveal the dislocation density increase in the initial loading cycles until the formation of sub-grain structures in the ferrite grains.

The grain-based GROD analysis in Fig. 16 reveals the change of grain misorientation with strain amplitudes and loading cycles. As is shown in the GROD distribution of Fig. 16 (a) and (b), the increasing strain amplitudes from 0.008 to 0.02 promote a steady increase in grain misorientation. On the other hand, Fig. 16 (c) and (d) show that the GROD distribution does not change from the 5th to the 30th cycle, but a shift of GROD distribution peak is observed from 0° ~ 1° at the 30th cycle to 1° ~ 2° at the 300th cycle. In addition, the small distribution change from

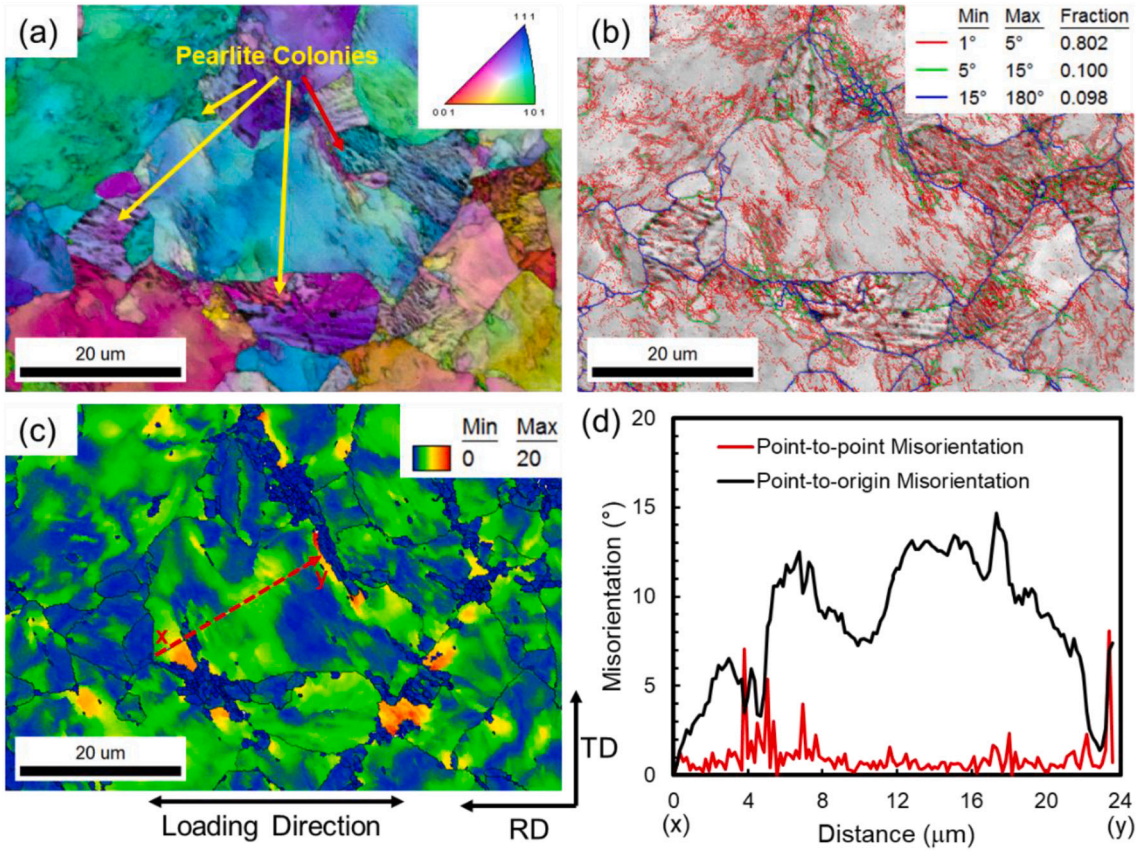

Fig. 11. Strain localization of ferritic-pearlitic microstructure under 0.02 strain amplitude. (a) IPF & IQ image (b) Grain boundary image (c) GROD image and misorientation line analysis x-y within a ferrite grain. (d) Misorientation along the xy line. Strain localization is observed at the ferrite-pearlite interface next to a pearlite grain (pointed by the red arrow) with significant strain accumulation. The IPF map was plotted in the ND direction. (For interpretation of the references to colour in this figure legend, the reader is referred to the web version of this article.)

the 300th cycle to the 667th cycle indicates that the accumulation of the loading cycles shows little impact on the grain misorientation after stabilization. Compared with the distribution of KAM in Fig. 15 (b) and (d), the GROD distributions of fatigue and interrupted test samples do not exhibit the distinction between the ferrite grains and the pearlite colonies. In contrast, the KAM distinction between the ferrite and pearlite peaks is attributed to the local misorientation at the pre-existing ferrite-cementite interface. However, the local misorientation due to the interface could not be reflected in the GROD distribution. The correlations between the Taylor factor and the grain misorientation are shown in Fig. 16 (b) and (d). The results indicate that grains with a lower Taylor factor tend to exhibit a higher average GROD value, but the GROD difference is insignificant. Therefore, the impact of the Taylor factor on strain distribution is less critical in this study. In addition, Fig. 16 (b) and (d) demonstrate that the average GROD value increases significantly with strain amplitudes, but the GROD increase with loading cycles is less significant.

4.2. Plastic behavior and strain localization of ferritic-Pearlitic microstructure

According to the EBSD analysis results, the plastic strain accumulates in the vicinity of ferrite-pearlite interfaces. The strain partitioning occurs due to the strength incompatibility between ferrite grains and pearlite colonies, as is shown in Fig. 8. The strain localization strengthens the material during plastic deformation but compromises the ductility simultaneously. Karlson and Linden showed that carbon steels with harder pearlite exhibit higher flow stress than the ones with softer pearlite [1]. Basantia et al. demonstrated that ferritic-pearlitic steels possess less yield and tensile strength but more significant elongation than the ferrite-bainite and ferrite-martensite steels, which exhibit larger microstructure incompatibilities than the ferritic-pearlitic steel [13]. The strain hardening of the ferrite phase is affected by the mean free path of dislocations limited by the cementite layers in pearlite colonies and the grain boundaries in the ferrite grains [15]. The barrier of cementite interlayers leads to the pileup of dislocations at ferrite-cementite interfaces and strengthens the pearlite colonies [15]. Pearlite colonies with smaller inter-lamellar spacing show a more substantial strain hardening rate during plastic deformation than the ones with larger inter-lamellar spacing [12,56,57]. The strain distribution of pearlite colonies is also affected by the angle between the lamellar alignment and the loading direction, as the most significant deformation of pearlite occurs at a 45-degree angle [14,58,59]. During cyclic loading, the Bauschinger effect describes the decrease of flow stress with a reversed loading direction. So a backstress term is introduced to represent the change of flow stress under tension and compression. With a tensile prestrain added to the material, the tensile flow stress (σ_t) can be represented in a simple model [60] as

$$\sigma_t = \sigma_0 + \sigma_f + \sigma_b, \tag{1}$$

and the compressive flow stress (σ_c) can be represented as

$$\sigma_c = \sigma_0 + \sigma_f - \sigma_b, \tag{2}$$

where σ_0, σ_f, and σ_b represent the initial yield strength, Forrest hardening, and back stress, respectively. The generation of backstress is due to the long-range internal stresses formed by dislocation pileups [61]. The dislocation pileups at GB and the ferrite-cementite interface contribute to the internal stress formation in the ferrite-pearlite

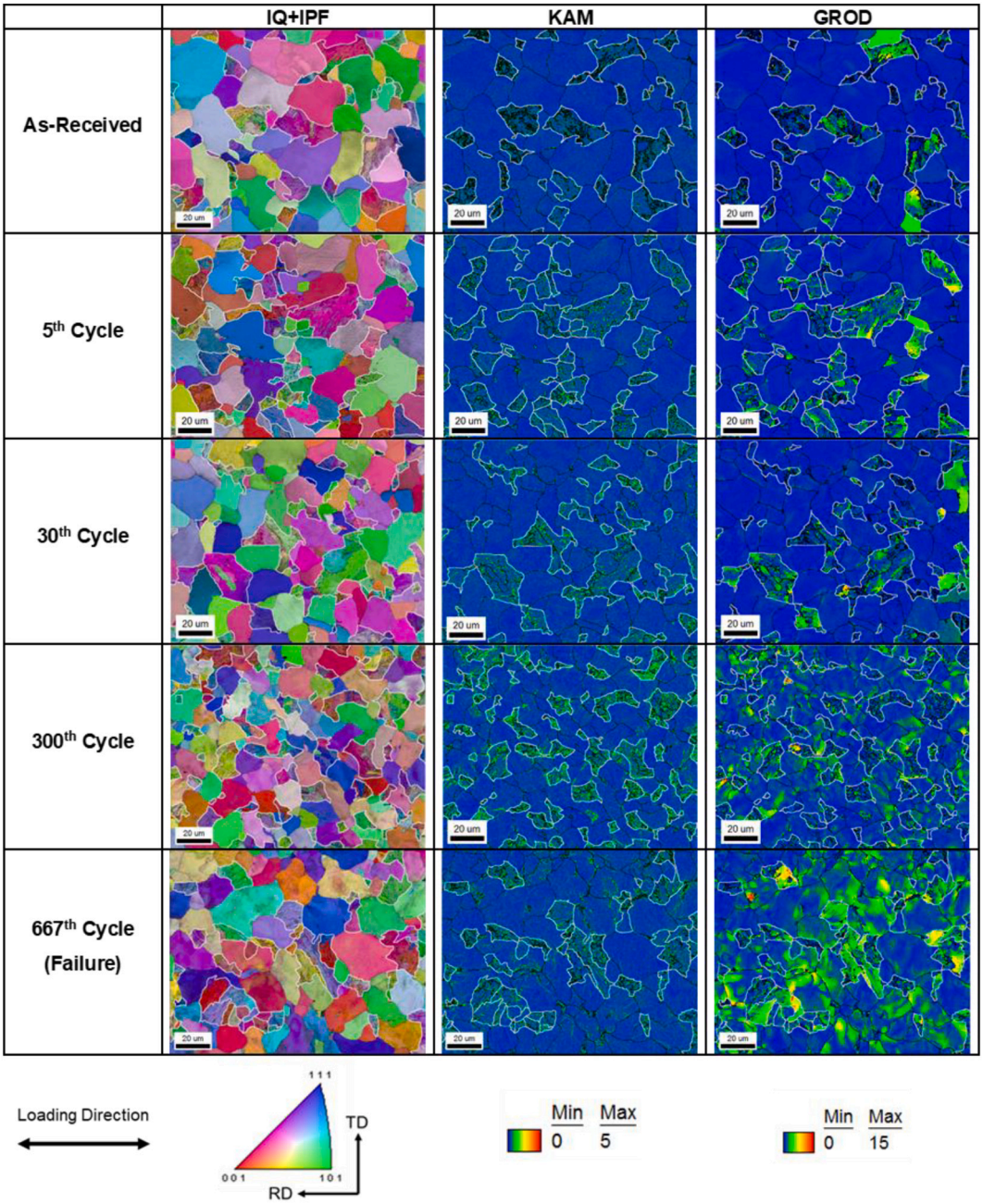

Fig. 12. IPF, KAM, and GROD of ferritic-pearlitic microstructures from As-Received sample and interrupted fatigue samples at the 5th Cycle, 30th Cycle, 300th Cycle, and 667th Cycle (Failure). The size of the scanning regions is 150 μm × 120 μm with 0.2 μm step size. Strain localization is observed at pearlite colonies and ferrite-pearlite interfaces. The accumulation of plastic strain increases with the cycles of ILCF loading. Pearlite colonies were outlined with white contour. IPF maps were plotted in the ND direction.

microstructure. In addition, incompatible microstructure constituents such as ferrite and pearlite increase the strain localization at GBs and enhance the Bauschinger effect [50,62,63].

According to the GROD analysis in Fig. 10, the strain localization indicated by orientation deviation shows an evident dependence upon the strain amplitudes of cyclic deformation. Multiple strain localization sites are observed in the ferrite grains of the 0.02 strain fatigue sample in contrast to the strain distribution of the 0.008 strain fatigue sample. The impact of strain amplitudes on cyclic deformation can be addressed from two perspectives: dislocation slip irreversibility and slip distance increasing. Suresh [60] pointed out that the dislocation motion in the BCC phase occurs back and forth on the same slip planes at low strain amplitudes, but the slip planes of to-and-fro dislocation motion become asymmetric at high strain amplitudes. On the former occasion, dislocation motion could be reversible without any barrier, so the long-range internal stresses within the microstructure does not occur. In contrast, high strain amplitude induces the irreversibility of dislocation motion and enhances the dislocation interaction and multiplication. In polycrystalline aggregates like the ferrite-pearlite microstructure, high strain amplitudes increase the triaxiality of internal stresses within grains, so multiple slip systems are activated to promote dislocation density [60]. The KAM and GROD analysis in Fig. 10 demonstrate that the 0.02 strain amplitude leads to a proliferation of GNDs, which induces significant lattice rotation in ferrite grains. High strain amplitude also increases the slip distance and thus promotes the dislocation pileup at GBs during forwarding motion. The subsequent piling-up dislocations then inhibit

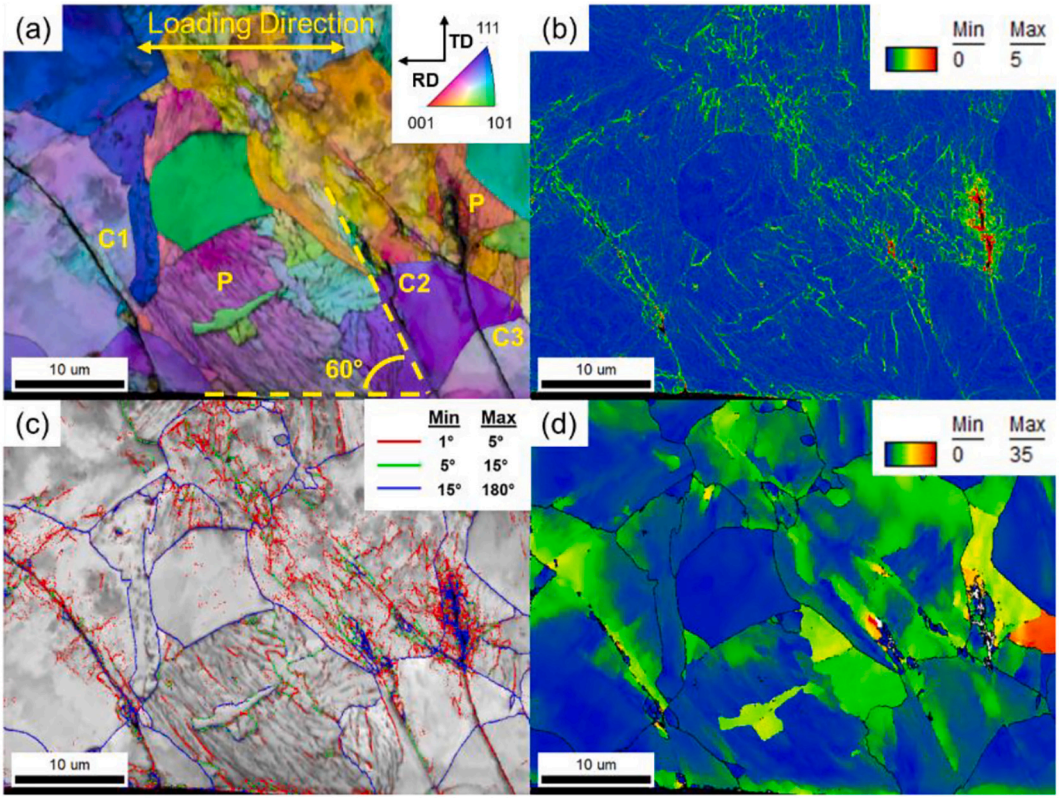

Fig. 13. Parallel short cracks propagation from the sample surface tested at 0.01 strain amplitude. (a) IPF and IQ figure (b) KAM image (c) Grain boundary and IQ figure (d) GROD image. C1, C2, and C3 cracks initated at the ferrite grains and grew along 60° to the loading direction. The strain localization along C3 in a pearlite grain indicates the plastic zone interaction between the crack tip and ferrite-cementite interfaces. The IPF map was plotted in the ND direction.

backward dislocation motion. As a result, the moving dislocations are trapped at the GBs and form strain localization sites. As shown in Fig. 11 (c) and (d), the plastic incompatibility between ferrite and pearlite further promotes strain localization in the vicinity of the interface. The ferrite grains surrounded by pearlite colonies are observed to possess higher KAM and GROD values than the grains among ferrite aggregate.

Strain localization due to microstructure incompatibility promotes the void nucleation close to the grain boundaries and accelerates crack propagation [13,18]. In addition, pearlite colonies increase the tortuosity of the crack path and improve the resistance to fatigue crack propagation. Many studies have well-demonstrated the deflection of crack growth by pearlite colonies, as the ferrite grains provide clear paths along the slip planes [27–30]. The plastic deformation at the crack tip could be enhanced in the vicinity of the ferrite-pearlite interface, as is shown in Fig. 14. The strain localization indicates the interaction between the plastic zone of the crack tip and the ferrite-pearlite interface. Higher plastic strain localization is observed along the crack path into a pearlite colony than along the crack path in ferrite grains, as is compared between the cracks C3 and C1 and C2 in Fig. 13 (a).

4.3. Correlation between Nanoindentation measurement and EBSD analysis

The nanoindentation technique can identify microstructures based on high-resolution mechanical property measurements [64–71]. Chang et al. showed that the nanoindentation measurements reveal hardness differences in complex phase steels and correlate well with the KAM image from EBSD analysis [40]. Furthermore, the nanoindentation measurement reveals local mechanical deformation due to dislocation density distribution, which can be reflected by EBSD analysis [72–76]. The nanoindentation measurements in Fig. 8 reveal that the cyclic deformation induces a significant increase in the hardness of ferrite grains and pearlite colonies. Interestingly, the ferrite hardness decreases with the increasing strain amplitudes, which contradicts the EBSD analysis results. However, it is noteworthy that KAM and GROD only reflect the GNDs distribution but ignore another type of dislocation known as Statistically Stored Dislocation (SSD). SSDs and GNDs are generated during plastic deformation, but SSDs are distributed randomly within the ferrite grains [61]. Schayes et al. pointed out that the limitation of EBSD analysis in measuring total dislocation density must be resolved using other techniques [36]. Rui et al. [77] demonstrated that SSDs are more dominant than GNDs among the dislocations in cyclically-deformed low-alloy steel. Nanoindentation measurement is an approach to investigate the strain hardening induced by dislocation multiplications. Durst et al. [78] summarized the relationship between hardness and the densities of SSDs and GNDs in Ni—Fe alloys as

$$H = H_{SSL} + MC\alpha Gb\sqrt{\rho_{SSD}(\varepsilon_{rep}) + \rho_{GND}(h)}, \quad (3)$$

where H_{SSL} represents the alloy-inherited hardness from solid-solutioning. ρ_{SSD} and ρ_{GND} are the dislocation density of SSDs and GNDs in a function of plastic strain (ε_{rep}) and indentation depth (h), respectively. Material constants include Taylor factor (M), shear modulus (G), and Burger vector magnitude (b). α and C represent the dislocation interaction constant (~ 0.5) and the indentation factor (~ 3).

Grain-based KAM and GROD analysis show the GND density increases significantly with strain amplitudes. Therefore, the hardness decrease with strain amplitudes indicates that the ferrite grains in the low-strain fatigue samples possess a higher amount of SSDs than in the ferrite grains of the high-strain fatigue samples. Furthermore, Table 3 shows that the total accumulative plastic strain decreases with the strain amplitudes. The saturation of dislocation density should coincide with the stabilization of cyclic flow stress at approximately half of the fatigue

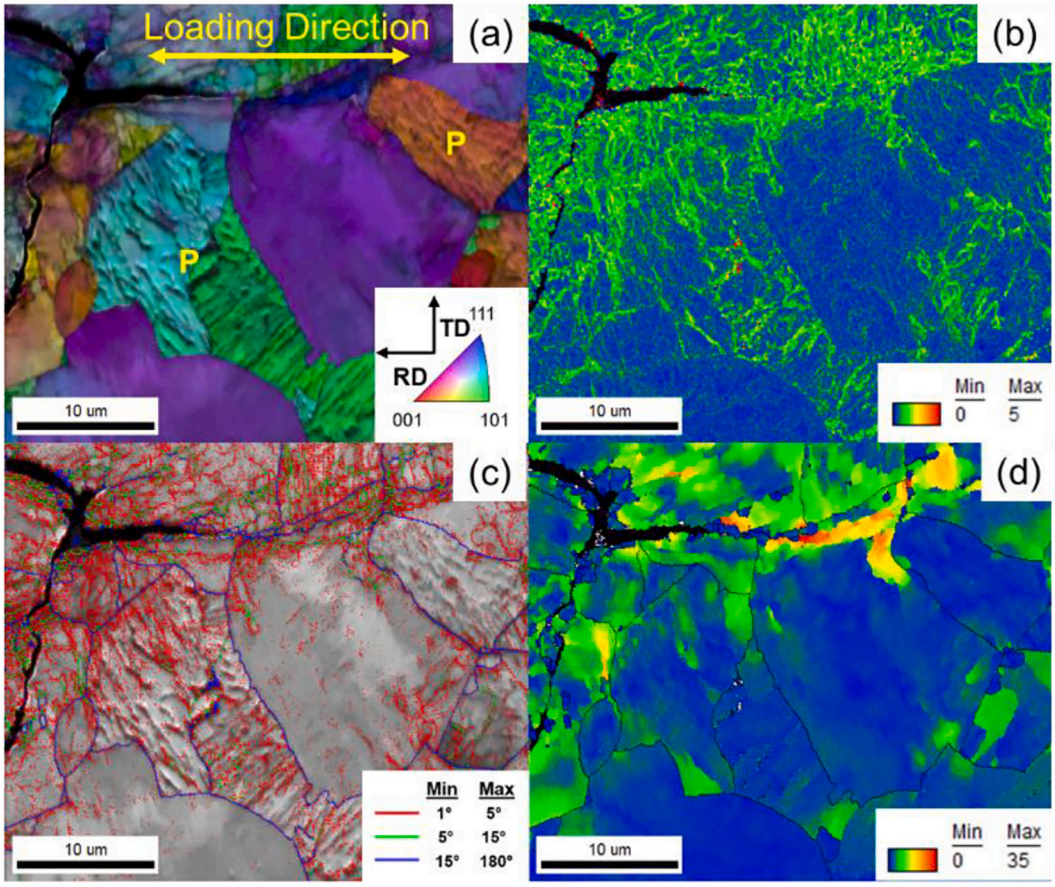

Fig. 14. Crack propagation and strain localization between the crack path and the ferrite-pearlite interface tested at 0.01 strain amplitude. (a) IPF and IQ figure (b) KAM image (c) Grain boundary and IQ figure (d) GROD figure. The significant strain localization indicates the interaction between the crack plastic zone and the ferrite-pearlite interface. The IPF map was plotted in the ND direction.

life, so the accumulative plastic strain until saturation supports that the ferrite grains in the fatigue sample at 0.008 strain possess the largest amount of SSDs density. Under the same strain amplitude, the ferrite hardness of interrupted samples increases along with cycles in Fig. 9 (b), revealing the impact of accumulative plastic strain on dislocation density and microstructure hardness. In this case, the GNDs and the SSDs of interrupted samples increase simultaneously with loading cycles; hence the nanoindentation measurement is consistent with the EBSD results. In addition, the hardness of pearlite colonies also decreases with strain amplitudes, but the hardness uncertainty is more significant than that of ferrite grains. The error bars of ferrite hardness in Fig. 8 indicate that the significant hardness uncertainty in the fatigue samples is attributed to the cyclic deformation. In contrast, the consistent hardness uncertainty in the pearlite colonies of the as-received and fatigue samples is caused by various pearlite morphologies. As the hard phases like cementite significantly increase the measured hardness value, the uncertainty of pearlite hardness could be affected by the factors such as cementite thickness and interlamellar spacing.

As is shown in Fig. 9 (b), the hardness of ferrite-pearlite microstructure increases with accumulative plastic strain from 0th to 300th cycle at 0.01 strain amplitude. Compared with the steady hardness increase over cycles in the pearlite colonies, the most significant hardness increase in ferrite grains occur within the first 30 cycles. The ferrite hardness increase coincides with the cyclic stress response change shown in Fig. 9 (a), indicating that the strain hardening of ferrite grains plays a crucial role in determining the cyclic stress response. Nevertheless, the pearlite hardness does not reflect the temporary softening from the 5th cycle to the 30th cycle, as is shown in Fig. 15 (c). From the 30th to the 300th cycle, both microstructure constituents exhibit a steady hardness increase, which agrees with the corresponding cyclic stress response. However, the discrepancy between hardness and cyclic stress response is observed at the 667th cycle, when the microstructure hardness is slightly lower than the hardness at the 300th cycle. From the stabilized stage to failure, the hardness decreasing trend is likely caused by the dislocation annihilation and rearrangement, while the cyclic hardening response is related to a strong strain localization at the ferrite GBs. The strain localization is supported by the GROD images in Fig. 12, as the orientation deviation of ferrite grains increases in the vicinity of ferrite-pearlite interfaces at 0.02 strain. It is noteworthy that the nanoindentation measurements only reveal the strain hardnening effect within grains, while the indents at GBs were not included in the analysis due to the spatial resolution.

The nanoindenation measurements can well complement the EBSD analysis to evaluate the plastic deformation in the ferrite-pearlite microstructure. While EBSD analysis is a powerful approach to capture the microstructure change due to plastic deformation, nanoindentation measurement is proven efficient in evaluating the total dislocation density that contributes to the cyclic hardening response. Nevertheless, spatial resolution is another crucial difference between the two approaches [34]. The large spatial resolution of the nanoindentation measurements brings significant uncertainties to the hardness of pearlite colonies. It is also not recommended to use nanoindentation to evaluate the strain localization at the GBs, as the hardening is more likely caused by the high dislocation density at the GBs rather than the dislocations in the adjacent ferrite region.

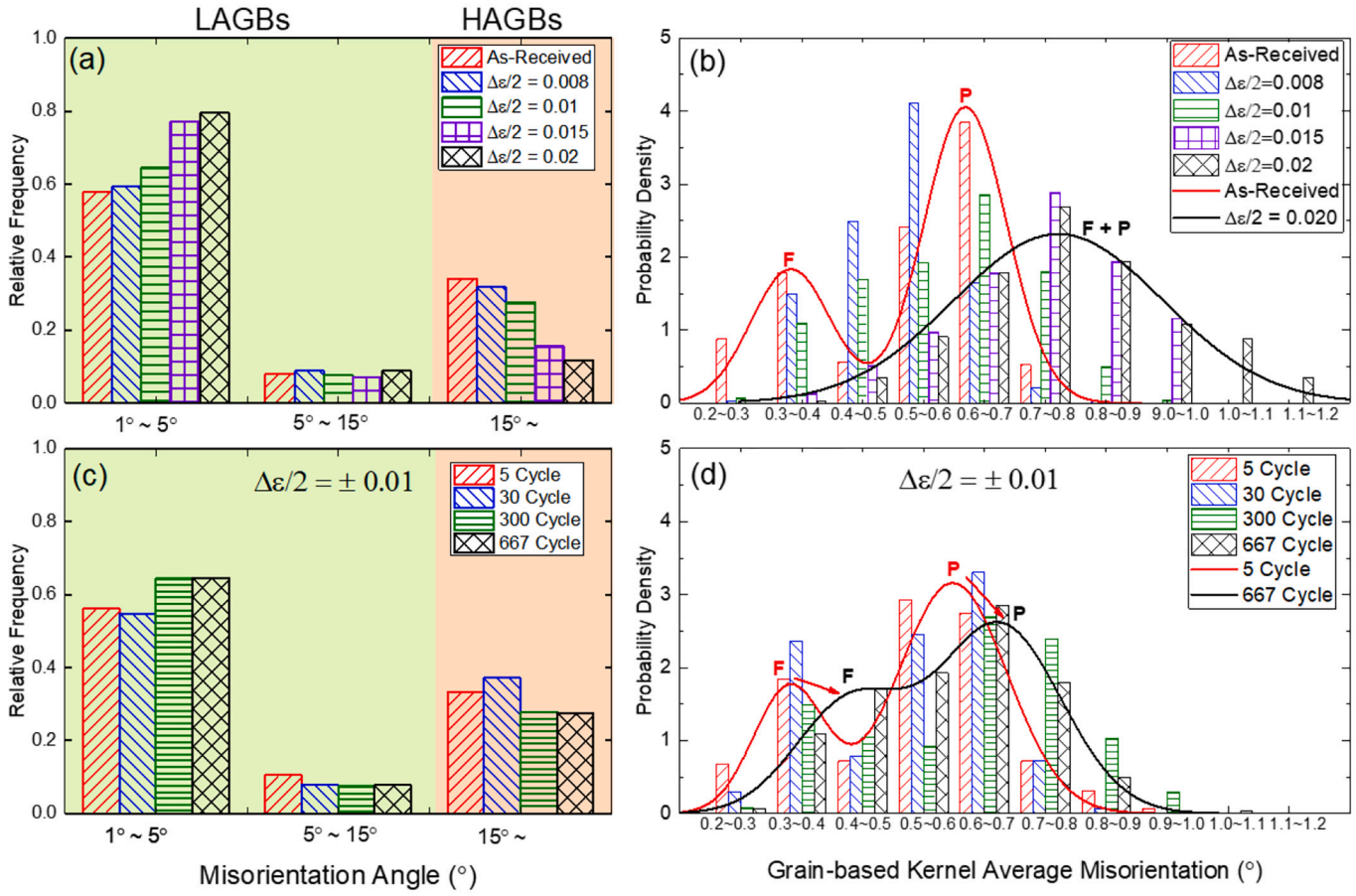

Fig. 15. Statistical summary of misorientation under different strain amplitudes and life cycles. (a) Relative frequencies of misorientation angle in the As-Received and the fatigue samples tested at 0.008, 0.01, 0.015, and 0.02 plastic strain amplitude. (b) Probability density of grain-based average KAM of the ferritic-pearlitic microstructure under different ILCF strain amplitudes. (c) Relative frequencies of misorientation angle in the interrupted fatigue samples at the 5th, 30th, 300th, and 667th cycles. (d) Probability density of grain-based average KAM at different life cycles.

5. Conclusions

This study comprehensively evaluates the cyclic deformation in a ferritic-pearlite low-alloy steel using OM, SEM, EBSD, and nano-indentation measurements. Microstructural deformation was evaluated under different strain amplitudes and loading cycles using the grain-based KAM and GROD analysis. The conclusions are summarized below.

- The misorientation due to plastic deformation increases with strain amplitudes ranging from 0.008 to 0.02. Strain localization is observed at the ferrite-cementite interfaces and ferritic-pearlitic grain boundaries due to the microstructure incompatibility. Nevertheless, the misorientation distribution becomes homogeneous in the 0.02 strain sample.
- The microstructure misorientation analysis of interrupted test samples shows that the plastic strain accumulates with loading cycles. Strain localization is mainly observed in the pearlite colonies before the stabilization of cyclic stress. After the stabilized cycle, strain localization is observed in the pearlite colonies and the vicinity of ferrite grain boundaries.
- Fatigue crack propagation is observed in the ferrite grains along the slip plane directions and deflected by GBs. The plastic zone at the crack tip enhances the ferrite-pearlite strain partitioning and induces the strain localization at the GBs.
- Grain-based average GROD and KAM in ferrite grains and pearlite colonies exhibit an increase with strain amplitudes and loading cycles. Cyclic deformation reduces the grain-based KAM difference in ferrite and pearlite, and the KAM difference diminishes in the fatigue samples tested at 0.015 and 0.02 strain amplitudes.
- KAM and GROD analysis of fatigue samples demonstrate that high strain amplitudes promote the GND density and strain localization in the vicinity of GBs. The incompatibility between neighboring ferrite grains and pearlite colonies leads to a further enhancement of strain localization at the ferrite-pearlite interface.
- The nanoindentation measurements indicate that the SSD density in ferrite grains increases with the plastic strain accumulation during cyclic deformation.
- The combination of EBSD analysis and nanoindentation successfully reveals the microstructural evolution over cycles: significant cyclic hardening of ferrite grains from 0th to 30th cycle; temporary softening of pearlite colonies from the 5th to the 30th cycle; steady cyclic hardening in ferrite and pearlite occurs during the 30th to the 300th cycle; re-arrangement and annihilation of dislocations in the ferrite-pearlite microstructure and enhancement of strain localization at the GBs from the 300th cycle to failure.

Data availability

The raw/processed data required to reproduce these findings cannot be shared at this time as the data also forms part of an ongoing study.

Declaration of Competing Interest

The authors declare that they have no known competing financial interests or personal relationships that could have appeared to influence

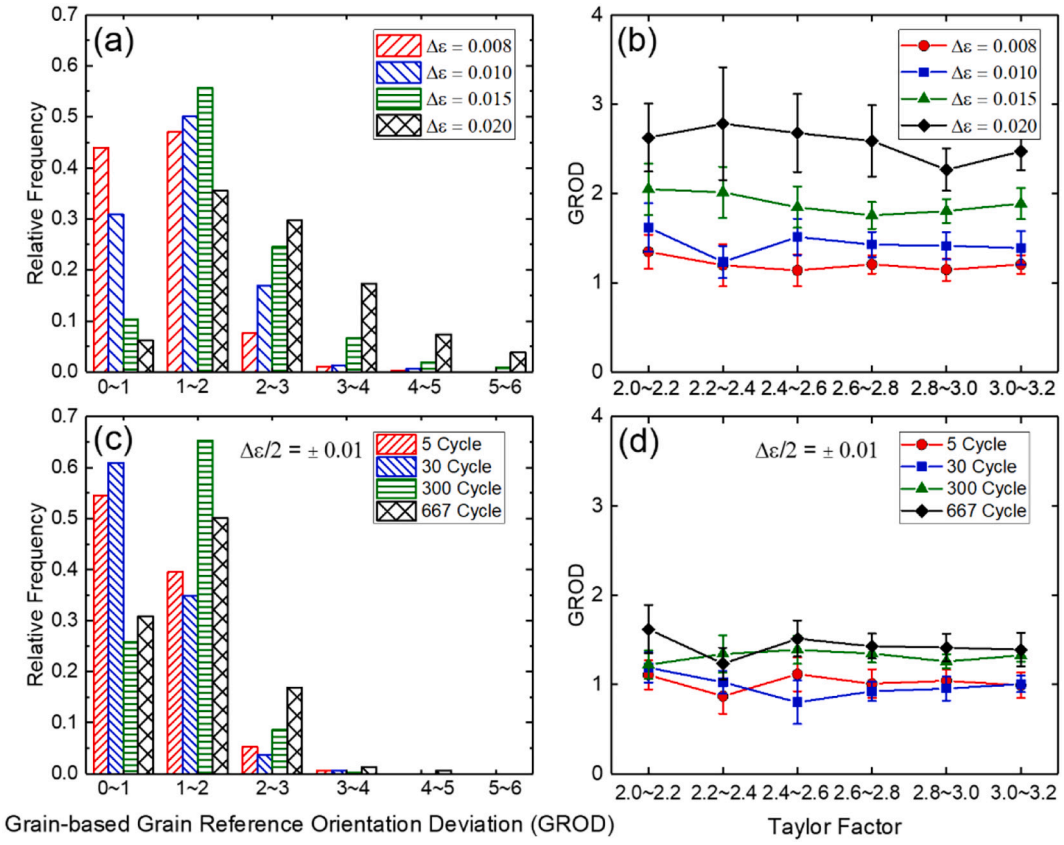

Fig. 16. Statistical summary of grain-based GROD analysis and its correlation with the Taylor factor. (a) Grain-based GROD distribution in the fatigue samples. (b) Correlation between Taylor factor and GROD in the fatigue samples. (c) Grain-based GROD distribution in the interrupted fatigue samples tested at 0.01 strain amplitude. (d) Correlation between Taylor factor and GROD during cyclic loading. The error bars indicate a 95% confidence interval of the GROD values.

the work reported in this paper.

Data availability

The authors do not have permission to share data.

Acknowledgement

The project is funded by the Manufacturing and Materials Joining Innovation Center (MA^2JIC) at the Ohio State University, supported by the National Science Foundation Industry University Cooperative Research Center program (IUCRC) (NSF 2052747). The authors would like to acknowledge the support from the Center for Electron Microscopy and Analysis (CEMAS) at the Ohio State University for providing advanced characterization facility.

References

[1] B. Karlsson, G. Lindén, Plastic deformation of ferrite—pearlite structures in steel, Mater. Sci. Eng. 17 (2) (Feb. 1975) 209–219, https://doi.org/10.1016/0025-5416(75)90232-3.
[2] J.D. Verhoeven, A review of microsegregation induced banding phenomena in steels, J. Mater. Eng. Perform. 9 (3) (Jun. 2000) 286–296, https://doi.org/10.1361/105994900770345935.
[3] R. Feng, S. Li, X. Zhu, Q. Ao, Microstructural characterization and formation mechanism of abnormal segregation band of hot rolled ferrite/pearlite steel, J. Alloys Compd. 646 (Oct. 2015) 787–793, https://doi.org/10.1016/j.jallcom.2015.05.128.
[4] S.W. Thompson, P.R. Howell, Factors influencing ferrite/pearlite banding and origin of large pearlite nodules in a hypoeutectoid plate steel, Mater. Sci. Technol. 8 (9) (Sep. 1992) 777–784, https://doi.org/10.1179/mst.1992.8.9.777.
[5] S.E. Offerman, N.H. van Dijk, M.Th. Rekveldt, J. Sietsma, S. van der Zwaag, Ferrite/pearlite band formation in hot rolled medium carbon steel, Mater. Sci. Technol. 18 (3) (Mar. 2002) 297–303, https://doi.org/10.1179/026708301225000752.
[6] F.A. Khalid, M. Farooque, A. ul Haq, A.Q. Khan, Role of ferrite/pearlite banded structure and segregation on mechanical properties of microalloyed hot rolled steel, Mater. Sci. Technol. 15 (10) (Oct. 1999) 1209–1215, https://doi.org/10.1179/026708399101505121.
[7] Y.B. Xu, Y.L. Bai, Q. Xue, L.T. Shen, Formation, microstructure and development of the localized shear deformation in low-carbon steels, Acta Mater. 44 (5) (May 1996) 1917–1926, https://doi.org/10.1016/1359-6454(95)00306-1.
[8] R.A. Jaramillo, M.T. Lusk, Dimensional anisotropy during phase transformations in a chemically banded 5140 steel. Part II: modeling, Acta Mater. 52 (4) (Feb. 2004) 859–867, https://doi.org/10.1016/j.actamat.2003.10.020.
[9] R.A. Grange, Effect of microstructural banding in steel, Metall. Trans. A. 2 (2) (Feb. 1971) 417–426, https://doi.org/10.1007/BF02663328.
[10] S. Isavand, A. Assempour, Effects of microstructural morphology on formability, strain localization, and damage of ferrite-pearlite steels: experimental and micromechanical approaches, Metall. Mater. Trans. A 52 (2) (Feb. 2021) 711–725, https://doi.org/10.1007/s11661-020-06115-2.
[11] S.A. Parsons, D.V. Edmonds, Microstructure and mechanical properties of medium-carbon ferrite–pearlite steel microalloyed with vanadium, Mater. Sci. Technol. 3 (11) (Nov. 1987) 894–904, https://doi.org/10.1179/mst.1987.3.11.894.
[12] V.I. Izotov, V.A. Pozdnyakov, E.V. Luk'yanenko, O.Yu. Usanova, G.A. Filippov, Influence of the pearlite fineness on the mechanical properties, deformation behavior, and fracture characteristics of carbon steel, Phys. Met. Metallogr. 103 (5) (May 2007) 519–529, https://doi.org/10.1134/S0031918X07050122.
[13] S.K. Basantia, A. Bhattacharya, N. Khutia, D. Das, Plastic Behavior of Ferrite–Pearlite, Ferrite–Bainite and Ferrite–Martensite Steels: Experiments and Micromechanical Modelling, Met. Mater. Int. 27 (5) (May 2021) 1025–1043, https://doi.org/10.1007/s12540-019-00519-5.
[14] S. Isavand, A. Assempour, Strain localization and deformation behavior in ferrite-pearlite steel unraveled by high-resolution in-situ testing integrated with crystal plasticity simulations, Int. J. Mech. Sci. 200 (Jun. 2021), 106441, https://doi.org/10.1016/j.ijmecsci.2021.106441.
[15] T. Takahashi, M. Nagumo, Flow stress and work-hardening of Pearlitic steel, Trans. Jpn. Inst. Metals 11 (2) (1970) 113–119, https://doi.org/10.2320/matertrans1960.11.113.
[16] B.E. Q'Donnelly, R.L. Reuben, T.N. Baker, Quantitative assessment of strengthening parameters in ferrite-pearlite steels from microstructural measurements, Met. Technol. 11 (1) (Jan. 1984) 45–51, https://doi.org/10.1179/030716984803274837.
[17] Y. Zhang, et al., Fatigue behaviour of a multiphase medium carbon steel: comparison between ferrite/pearlite and tempered microstructures, Fatigue Fract.

Eng. Mater. Struct. 43 (11) (Nov. 2020) 2542–2549, https://doi.org/10.1111/ffe.13274.
[18] K. Noh, S.A.A. Shams, W. Kim, J.N. Kim, C.S. Lee, Influence of microstructure on low-cycle and extremely-low-cycle fatigue resistance of low-carbon steels, Met. Mater. Int. 27 (10) (Oct. 2021) 3862–3874, https://doi.org/10.1007/s12540-020-00819-1.
[19] M. Zecevic, Y.P. Korkolis, T. Kuwabara, M. Knezevic, Dual-phase steel sheets under cyclic tension–compression to large strains: experiments and crystal plasticity modeling, J. Mech. Phys. Solids 96 (Nov. 2016) 65–87, https://doi.org/10.1016/j.jmps.2016.07.003.
[20] N. Narasaiah, K.K. Ray, Small crack formation in a low carbon steel with banded ferrite–pearlite structure, Mater. Sci. Eng. A 392 (1–2) (Feb. 2005) 269–277, https://doi.org/10.1016/j.msea.2004.09.058.
[21] C. Liu, R. Ren, D. Liu, X. Zhao, C. Chen, An EBSD investigation on the evolution of the surface microstructure of D2 wheel steel during rolling contact fatigue, Tribol. Lett. 68 (1) (Mar. 2020) 47, https://doi.org/10.1007/s11249-020-1277-1.
[22] S. Sankaran, V.S. Sarma, K.A. Padmanabhan, Low cycle fatigue behavior of a multiphase microalloyed medium carbon steel: comparison between ferriteÁ/pearlite and quenched and tempered microstructures, Mater. Sci. Eng. A (2003) 8.
[23] V. Subramanya Sarma, Low cycle fatigue behaviour of a medium carbon microalloyed steel, Int. J. Fatigue 19 (2) (1997) 135–140, https://doi.org/10.1016/S0142-1123(96)00060-6.
[24] S. Sankaran, V. Subramanya Sarma, K.A. Padmanabhan, G. Jaeger, A. Koethe, High cycle fatigue behaviour of a multiphase microalloyed medium carbon steel: a comparison between ferrite–pearlite and tempered martensite microstructures, Mater. Sci. Eng. A 362 (1–2) (Dec. 2003) 249–256, https://doi.org/10.1016/S0921-5093(03)00583-5.
[25] S. Suresh, Crack deflection: implications for the growth of long and short fatigue cracks, Metall. Trans. A. 14 (11) (Nov. 1983) 2375–2385, https://doi.org/10.1007/BF02663313.
[26] M. Guan, H. Yu, Fatigue crack growth behaviors in hot-rolled low carbon steels: a comparison between ferrite–pearlite and ferrite–bainite microstructures, Mater. Sci. Eng. A 559 (Jan. 2013) 875–881, https://doi.org/10.1016/j.msea.2012.09.036.
[27] M.S. Mustapa, Y. Mutoh, Effects of size and spacing of uniformly distributed pearlite particles on fatigue crack growth behavior of ferrite–pearlite steels, Mater. Sci. Eng. A 527 (10–11) (Apr. 2010) 2592–2597, https://doi.org/10.1016/j.msea.2009.12.023.
[28] A.A. Korda, Y. Mutoh, Y. Miyashita, T. Sadasue, Effects of pearlite morphology and specimen thickness on fatigue crack growth resistance in ferritic–pearlitic steels, Mater. Sci. Eng. A 428 (1–2) (Jul. 2006) 262–269, https://doi.org/10.1016/j.msea.2006.05.015.
[29] A. Korda, Y. Miyashita, Y. Mutoh, T. Sadasue, Fatigue crack growth behavior in ferritic–pearlitic steels with networked and distributed pearlite structures, Int. J. Fatigue 29 (6) (Jun. 2007) 1140–1148, https://doi.org/10.1016/j.ijfatigue.2006.09.008.
[30] A.A. Korda, Y. Mutoh, Y. Miyashita, T. Sadasue, S.L. Mannan, In situ observation of fatigue crack retardation in banded ferrite–pearlite microstructure due to crack branching, Scr. Mater. 54 (11) (Jun. 2006) 1835–1840, https://doi.org/10.1016/j.scriptamat.2006.02.025.
[31] S. Wroński, J. Tarasiuk, B. Bacroix, A. Baczmański, C. Braham, Investigation of plastic deformation heterogeneities in duplex steel by EBSD, Mater. Charact. 73 (Nov. 2012) 52–60, https://doi.org/10.1016/j.matchar.2012.07.016.
[32] W. Li, H. Gao, H. Nakashima, S. Hata, W. Tian, In-situ EBSD study of deformation behavior of retained austenite in a low-carbon quenching and partitioning steel via uniaxial tensile tests, Mater. Charact. 118 (Aug. 2016) 431–437, https://doi.org/10.1016/j.matchar.2016.06.020.
[33] H. Mirzadeh, J.M. Cabrera, A. Najafizadeh, P.R. Calvillo, EBSD study of a hot deformed austenitic stainless steel, Mater. Sci. Eng. A 538 (Mar. 2012) 236–245, https://doi.org/10.1016/j.msea.2012.01.037.
[34] D.N. Githinji, S.M. Northover, P.J. Bouchard, M.A. Rist, An EBSD study of the deformation of service-aged 316 austenitic steel, Metall. Mater. Trans. A 44 (9) (Sep. 2013) 4150–4167, https://doi.org/10.1007/s11661-013-1787-7.
[35] G. Maistro, C. Oikonomou, L. Rogström, L. Nyborg, Y. Cao, Understanding the microstructure-properties relationship of low-temperature carburized austenitic stainless steels through EBSD analysis, Surf. Coat. Technol. 322 (Aug. 2017) 141–151, https://doi.org/10.1016/j.surfcoat.2017.05.036.
[36] C. Schayes, A comparison of EBSD based strain indicators for the study of Fe-3Si steel subjected to cyclic loading, Mater. Charact. (2016) 10.
[37] S.-S. Rui, et al., EBSD analysis of cyclic load effect on final misorientation distribution of post-mortem low alloy steel: a new method for fatigue crack tip driving force prediction, Int. J. Fatigue 113 (Aug. 2018) 264–276, https://doi.org/10.1016/j.ijfatigue.2018.04.016.
[38] Y. Rae, X. Guo, A. Benaarbia, N. Neate, W. Sun, On the microstructural evolution in 12% Cr turbine steel during low cycle fatigue at elevated temperature, Mater. Sci. Eng. A 773 (Jan. 2020), 138864, https://doi.org/10.1016/j.msea.2019.138864.
[39] U. Mayo, N. Isasti, J.M. Rodríguez-Ibabe, P. Uranga, Analysis of strain partitioning in Intercritically deformed microstructures via interrupted tensile tests, Metals 11 (1) (Jan. 2021) 112, https://doi.org/10.3390/met11010112.
[40] Y. Chang, M. Lin, U. Hangen, S. Richter, C. Haase, W. Bleck, Revealing the relation between microstructural heterogeneities and local mechanical properties of complex-phase steel by correlative electron microscopy and nanoindentation characterization, Mater. Des. 203 (May 2021), 109620, https://doi.org/10.1016/j.matdes.2021.109620.
[41] M. Dollar, I.M. Bernstein, M. Daeubler, A.W. Thompson, The effect of cyclic loading on the dislocation structure of fully pearlitic steel, Metall. Trans. A. 20 (3) (Mar. 1989) 447–451, https://doi.org/10.1007/BF02653924.
[42] J. Kang, X. Liu, Ultrasonic effect on the deformation behavior and microstructure evolution of a TRIP-assisted steel, Metall. Mater. Trans. A 52 (10) (Oct. 2021) 4468–4478, https://doi.org/10.1007/s11661-021-06398-z.
[43] ASME, *boiler and pressure vessel code section II part A- ferrous material Specificiations (beginning to SA-450)*, ASME (2010) 301–303.
[44] Z. Xia, F. Ju, P. Du Plessis, Heat transfer and stress analysis of coke drum for a complete operating cycle, J. Press. Vessel. Technol. 132 (5) (Oct. 2010), 051205, https://doi.org/10.1115/1.4001208.
[45] T. Yamamoto, K. Arii, S. Niimoto, M. Ohata, T. Tagawa, F. Minami, Investigation of bulging behavior of coke drum—a practical analysis of bulging under complex quench conditions, J. Press. Vessel. Technol. 136 (6) (Dec. 2014), 061401, https://doi.org/10.1115/1.4027591.
[46] F. Ju, J. Aumuller, Zihui Xia, P. Du Plessis, Global and local elastic-plastic stress analysis of coke drum under thermal-mechanical loadings, J. Press. Vessel. Technol. 133 (6) (Dec. 2011) 061202, https://doi.org/10.1115/1.4002802.
[47] C.A. Schneider, W.S. Rasband, K.W. Eliceiri, NIH image to ImageJ: 25 years of image analysis, Nat. Methods 9 (7) (Jul. 2012) 671–675, https://doi.org/10.1038/nmeth.2089.
[48] R.A. Jaramillo, M.T. Lusk, M.C. Mataya, Dimensional anisotropy during phase transformations in a chemically banded 5140 steel. Part I: experimental investigation, Acta Mater. 52 (4) (Feb. 2004) 851–858, https://doi.org/10.1016/j.actamat.2003.11.017.
[49] T.A. Kop, J. Sietsma, S. van der Zwaag, Anisotropic dilatation behaviour during transformation of hot rolled steels showing banded structure, Mater. Sci. Technol. 17 (12) (Dec. 2001) 1569–1574, https://doi.org/10.1179/026708301101509629.
[50] M. Erdogan, R. Priestner, Effect of martensite content, its dispersion, and epitaxial ferrite content on Bauschinger behaviour of dual phase steel, Mater. Sci. Technol. 18 (4) (Apr. 2002) 369–376, https://doi.org/10.1179/026708302225001679.
[51] D.E. Martin, An energy criterion for low-cycle fatigue, J. Basic Eng. 83 (4) (Dec. 1961) 565–571, https://doi.org/10.1115/1.3662268.
[52] F. Ellyin, D. Kujawski, Plastic strain energy in fatigue failure, J. Press. Vessel. Technol. 106 (4) (Nov. 1984) 342–347, https://doi.org/10.1115/1.3264362.
[53] M.D. Callaghan, et al., Energy-based approach for the evaluation of low cycle fatigue behaviour of 2.25Cr–1Mo steel at elevated temperature, Mater. Sci. Eng. A 527 (21–22) (Aug. 2010) 5619–5623, https://doi.org/10.1016/j.msea.2010.05.011.
[54] O. Muránsky, L. Balogh, M. Tran, C.J. Hamelin, J.-S. Park, M.R. Daymond, On the measurement of dislocations and dislocation substructures using EBSD and HRSD techniques, Acta Mater. 175 (Aug. 2019) 297–313, https://doi.org/10.1016/j.actamat.2019.05.036.
[55] S.K. Paul, N. Stanford, T. Hilditch, Effect of martensite volume fraction on low cycle fatigue behaviour of dual phase steels: experimental and microstructural investigation, Mater. Sci. Eng. A 638 (Jun. 2015) 296–304, https://doi.org/10.1016/j.msea.2015.04.059.
[56] S. Allain, O. Bouaziz, Microstructure based modeling for the mechanical behavior of ferrite–pearlite steels suitable to capture isotropic and kinematic hardening, Mater. Sci. Eng. A 496 (1–2) (Nov. 2008) 329–336, https://doi.org/10.1016/j.msea.2008.06.009.
[57] L. Wang, D. Tang, Y. Song, Prediction of mechanical behavior of ferrite-pearlite steel, J. Iron Steel Res. Int. 24 (3) (Mar. 2017) 321–327, https://doi.org/10.1016/S1006-706X(17)30046-8.
[58] T. Teshima, M. Kosaka, K. Ushioda, N. Koga, N. Nakada, Local cementite cracking induced by heterogeneous plastic deformation in lamellar pearlite, Mater. Sci. Eng. A 679 (Jan. 2017) 223–229, https://doi.org/10.1016/j.msea.2016.10.018.
[59] B. Berisha, C. Raemy, C. Becker, M. Gorji, P. Hora, Multiscale modeling of failure initiation in a ferritic–pearlitic steel, Acta Mater. 100 (Nov. 2015) 191–201, https://doi.org/10.1016/j.actamat.2015.08.035.
[60] S. Suresh, Fatigue of Materials, Cambridge University Press, 1998.
[61] M.F. Ashby, The deformation of plastically non-homogeneous materials, Philos. Mag. J. Theor. Exp. Appl. Phys. 21 (170) (Feb. 1970) 399–424, https://doi.org/10.1080/14786437008238426.
[62] Y. Tomota, I. Tamura, Mechanical behavior of steels consisting of two ductile phases, Trans. Iron Steel Inst. Jpn. 22 (9) (1982) 665–677, https://doi.org/10.2355/isijinternational1966.22.665.
[63] ShIgenori Kumakura, The Bauschinger effect in carbon steels, Bull. JSME 11 (45) (1968) 426–436.
[64] B.-W. Choi, D.-H. Seo, J. Jang, A nanoindentation study on the micromechanical characteristics of API X100 pipeline steel, Met. Mater. Int. 15 (3) (Jun. 2009) 373–378, https://doi.org/10.1007/s12540-009-0373-4.
[65] M.D. Taylor, et al., Correlations between nanoindentation hardness and macroscopic mechanical properties in DP980 steels, Mater. Sci. Eng. A 597 (Mar. 2014) 431–439, https://doi.org/10.1016/j.msea.2013.12.084.
[66] T.-H. Pham, J.J. Kim, S.-E. Kim, Estimation of microstructural compositions in the weld zone of structural steel using nanoindentation, J. Constr. Steel Res. 99 (Aug. 2014) 121–128, https://doi.org/10.1016/j.jcsr.2014.04.011.
[67] E.A. Ariza-Echeverri, M. Masoumi, A.S. Nishikawa, D.H. Mesa, A.E. Marquez-Rossy, A.P. Tschiptschin, Development of a new generation of quench and partitioning steels: influence of processing parameters on texture, nanoindentation, and mechanical properties, Mater. Des. 186 (Jan. 2020), 108329, https://doi.org/10.1016/j.matdes.2019.108329.
[68] Y. Mazaheri, A. Kermanpur, A. Najafizadeh, Nanoindentation study of ferrite–martensite dual phase steels developed by a new thermomechanical

processing, Mater. Sci. Eng. A 639 (Jul. 2015) 8–14, https://doi.org/10.1016/j.msea.2015.04.098.
[69] V.H. Baltazar Hernandez, S.K. Panda, M.L. Kuntz, Y. Zhou, Nanoindentation and microstructure analysis of resistance spot welded dual phase steel, Mater. Lett. 64 (2) (Jan. 2010) 207–210, https://doi.org/10.1016/j.matlet.2009.10.040.
[70] B. Jiang, K. Doi, K. Tsuchiya, Y. Kawano, A. Kori, K. Ikushima, Micromechanical properties of steel corrosion products in concrete studied by nano-indentation technique, Corros. Sci. 163 (Feb. 2020), 108304, https://doi.org/10.1016/j.corsci.2019.108304.
[71] Q. Zhang, A.S.S. Singaravelu, Y. Zhao, T. Jing, N. Chawla, Mechanical properties of a thermally-aged cast duplex stainless steel by nanoindentation and micropillar compression, Mater. Sci. Eng. A 743 (Jan. 2019) 520–528, https://doi.org/10.1016/j.msea.2018.11.112.
[72] R. Lehnert, A. Weidner, M. Motylenko, H. Biermann, Strain hardening of phases in high alloy CrMnNi steel as a consequence of pre-deformation studied by nanoindentation, Adv. Eng. Mater. 21 (5) (2019).
[73] R.R. Shen, V. Ström, P. Efsing, Spatial correlation between local misorientations and nanoindentation hardness in nickel-base alloy 690, Mater. Sci. Eng. A 674 (Sep. 2016) 171–177, https://doi.org/10.1016/j.msea.2016.07.123.
[74] A. Fillafer, C. Krempaszky, E. Werner, On strain partitioning and micro-damage behavior of dual-phase steels, Mater. Sci. Eng. A 614 (Sep. 2014) 180–192, https://doi.org/10.1016/j.msea.2014.07.029.
[75] P.O. Guglielmi, M. Ziehmer, E.T. Lilleodden, On a novel strain indicator based on uncorrelated misorientation angles for correlating dislocation density to local strength, Acta Mater. 150 (May 2018) 195–205, https://doi.org/10.1016/j.actamat.2018.03.009.
[76] K.S. Mao, et al., Grain orientation dependence of nanoindentation and deformation-induced martensitic phase transformation in neutron irradiated AISI 304L stainless steel, Materialia 5 (Mar. 2019), 100208, https://doi.org/10.1016/j.mtla.2019.100208.
[77] S.-S. Rui, et al., Correlations between two EBSD-based metrics kernel average Misorientation and image quality on indicating dislocations of near-failure low alloy steels induced by tensile and cyclic deformations, Mater. Today Commun. 27 (Jun. 2021), 102445, https://doi.org/10.1016/j.mtcomm.2021.102445.
[78] K. Durst, O. Franke, A. Böhner, M. Göken, Indentation size effect in Ni–Fe solid solutions, Acta Mater. 55 (20) (Dec. 2007) 6825–6833, https://doi.org/10.1016/j.actamat.2007.08.044.